Ca^{2+} channel and active zone protein abundance intersects with input-specific synapse organization to shape functional synaptic diversity

Medeiros, A. T.[1], Gratz, S.J.[2*], Delgado, A.[2], Ritt, J.T.[2,3] and Kate M. O'Connor-Giles[1-3*]

[1] Neuroscience Graduate Training Program, Brown University, Providence, RI

[2] Department of Neuroscience, Brown University, Providence, RI

[3] Carney Institute for Brain Science, Brown University, Providence, RI

*For correspondence: Scott J. Gratz 185 Meeting St., Providence, RI 02912. email: scott_gratz@brown.edu; Kate M. O'Connor-Giles, 185 Meeting St., Providence, RI 02912. email: kate_oconnor-giles@brown.edu

The authors declare no competing interests.

ABSTRACT

Synaptic heterogeneity is a hallmark of nervous systems that enables complex and adaptable communication in neural circuits. To understand circuit function, it is thus critical to determine the factors that contribute to the functional diversity of synapses. We investigated the contributions of voltage-gated calcium channel (VGCC) abundance, spatial organization, and subunit composition to synapse diversity among and between synapses formed by two closely related *Drosophila* glutamatergic motor neurons with distinct neurotransmitter release probabilities (P_r). Surprisingly, VGCC levels are highly predictive of heterogeneous P_r among individual synapses of either low- or high-P_r inputs, but not between inputs. We find that the same number of VGCCs are more densely organized at high-P_r synapses, consistent with tighter VGCC-synaptic vesicle coupling. We generated endogenously tagged lines to investigate VGCC subunits *in vivo* and found that the α2δ-3 subunit Straightjacket along with the CAST/ELKS active zone (AZ) protein Bruchpilot, both key regulators of VGCCs, are less abundant at high-P_r inputs, yet positively correlate with P_r among synapses formed by either input. Consistently, both Straightjacket and Bruchpilot levels are dynamically increased across AZs of both inputs when neurotransmitter release is potentiated to maintain stable communication following glutamate receptor inhibition. Together, these findings suggest a model in which VGCC and AZ protein abundance intersects with input-specific spatial and molecular organization to shape the functional diversity of synapses.

46 **INTRODUCTION**

47 The broad and complex functions of neural circuits depend on diverse neuronal subtypes
48 communicating through synapses with distinct properties. Thus, understanding how synaptic diversity is
49 established is critical for understanding neural circuit function. Neurotransmission occurs at specialized
50 membranes called active zones (AZs) where action potentials drive the opening of voltage-gated Ca^{2+}
51 channels (VGCCs) to trigger Ca^{2+}-dependent synaptic vesicle (SV) fusion and neurotransmitter release.
52 Neurotransmitter release properties are determined locally at individual synapses and vary
53 considerably between neuronal subtypes and within homogeneous populations of neurons (Ariel,
54 Hoppa, and Ryan 2012; Atwood and Karunanithi 2002; Branco and Staras 2009; Hatt and Smith 1976).
55 In fact, functional imaging studies in *Drosophila* demonstrate that even single neurons forming
56 synapses with the same postsynaptic partner display heterogeneous synaptic strength among
57 individual AZs (Guerrero et al. 2005; Melom et al. 2013; Peled and Isacoff 2011).
58
59 Presynaptic strength is defined as the likelihood of neurotransmitter release following an action
60 potential (probability of release, P_r). This probabilistic process is determined by the number of functional
61 SV release sites and their individual probability of vesicle release. The probability of SV release is
62 highly dependent on transient increases in intracellular Ca^{2+} levels at vesicular sensors. Accordingly,
63 SV release sites and VGCCs are key substrates for generating diversity of synaptic function
64 (Akbergenova et al. 2018; Aldahabi et al. 2022; Chen et al. 2015; Fedchyshyn and Wang 2005; Fekete
65 et al. 2019; Gratz et al. 2019; Holderith et al. 2012; Laghaei et al. 2018; Miki et al. 2017; Nakamura et
66 al. 2015; Newman et al. 2022; Rebola et al. 2019; Reddy-Alla et al. 2017; Sauvola et al. 2021; Sheng et
67 al. 2012). Numerous studies have demonstrated that VGCC abundance is highly correlated with P_r
68 across species (Akbergenova et al. 2018; Gratz et al. 2019; Holderith et al. 2012; Miki et al. 2017;
69 Nakamura et al. 2015; Sheng et al. 2012). Paradoxically, this is not always the case. For example, a
70 recent study investigated two cerebellar synaptic subtypes, one high-P_r formed by inhibitory stellate
71 cells and one low-P_r formed by excitatory granule cells, and found higher VGCC levels at low-P_r
72 granule synapses (Rebola et al. 2019). Since VGCCs in closer proximity to release sites are expected

73 to have a greater impact on vesicular release probability than those positioned farther away, the spatial
74 coupling of VGCCs and SVs at AZs is a critical determinant of P_r (Chen et al. 2015; Eggermann et al.
75 2011; Fedchyshyn and Wang 2005; Nakamura et al. 2015; Rebola et al. 2019). Indeed, at high-P_r
76 stellate synapses, a 'perimeter release' AZ organization places VGCCs ~40nm closer to SVs than at
77 low-P_r granular synapses (Rebola et al. 2019). Another recent study investigated two functionally
78 distinct connections formed by CA1 pyramidal cells (Aldahabi et al. 2022). While Ca^{2+} influx was higher
79 at the high-P_r synapse, raising Ca^{2+} influx at the low-P_r synapse to match the high-P_r synapse did not
80 equalize P_r.
81
82 To further investigate this paradox, we sought a system where we could investigate the relationship
83 between VGCCs and P_r both within and between two closely related neurons that form synapses with
84 distinct release probabilities. *Drosophila* muscles are innervated by two glutamatergic motor neurons,
85 one tonic and one phasic, that form type Ib and type Is synapses, respectively. Type Ib synapses have
86 relatively low P_r and facilitate, whereas type Is synapses have higher P_r and depress in response to
87 high-frequency stimulation (Aponte-Santiago et al. 2020; Lnenicka and Keshishian 2000). In this study,
88 we investigated how VGCC abundance, spatial organization, and subunit composition contribute to
89 synaptic heterogeneity at AZs of low-P_r type Ib and high-P_r type Is inputs to the same postsynaptic
90 targets. We find that individual synapses formed by both low- and high-P_r inputs exhibit heterogeneous
91 release properties that can be predicted by VGCC abundance alone. However, VGCC abundance does
92 not correspond to differences in P_r between the two inputs. We identify underlying molecular and
93 organizational differences that may alter the relationship between VGCC abundance and P_r at low- vs.
94 high-P_r inputs. We further find that the homeostatic potentiation of neurotransmitter release triggered by
95 glutamate receptor inhibition involves dynamic increases in VGCCs, the α2δ-3 subunit Straightjacket
96 (Stj), and the AZ cytomatrix protein Bruchpilot (Brp) across AZs of both inputs. These findings provide
97 insight into how VGCC and AZ protein abundance intersects with underlying molecular and
98 organizational differences between inputs to contribute to greater synaptic diversity.

99

100 **RESULTS**

101 **VGCC levels predict P_r within, but not between, inputs**

102 To investigate the relationship between VGCC levels and neurotransmitter release properties at
103 functionally distinct synapses, we took advantage of the two motor neuron subtypes with low and high
104 release probabilities that innervate most *Drosophila* muscles (Aponte-Santiago and Littleton 2020;
105 Kurdyak et al. 1994). These glutamatergic neuromuscular junctions (NMJs) contain hundreds of
106 individual synapses that are accessible to single AZ functional imaging using genetically encoded Ca^{2+}
107 indicators.

108

109 In *Drosophila*, Cacophony (Cac) is the sole Ca_v2 pore-forming subunit and is the VGCC responsible for
110 triggering synaptic transmission (Kawasaki, Felling, and Ordway 2000; Macleod et al. 2006; Peng and
111 Wu 2007; Smith et al. 1996). To simultaneously monitor neurotransmitter release and VGCC levels, we
112 swapped the N-terminal sfGFP tag in our well-characterized $cac^{sfGFP\text{-}N}$ line for a Td-Tomato tag ($cac^{Td\text{-}}$
113 $^{Tomato\text{-}N}$) and confirmed that the tag does not impair synaptic function (Figs. 1A-F, S1; (Ghelani et al.
114 2023; Gratz et al. 2019)). We then expressed postsynaptically targeted GCaMP6f (SynapGCaMP6f;
115 (Newman et al. 2017)), which reports Ca^{2+} influx through glutamate receptors in response to
116 neurotransmitter release, in $cac^{Td\text{-}Tomato\text{-}N}$ animals for a plus/minus readout. We and others have
117 previously shown that Cac levels are highly predictive of P_r at individual type Ib AZs (Akbergenova et al.
118 2018; Gratz et al. 2019). To determine if VGCC levels are similarly predictive at high-P_r type Is AZs, we
119 measured $Cac^{Td\text{-}Tomato\text{-}N}$ fluorescence intensity and monitored neurotransmitter release in response to
120 0.2-Hz stimulus at individual synapses. To enable direct comparisons between the two inputs, we
121 simultaneously imaged type Ib and Is synapses at NMJ 6/7 (Fig. 1A). We quantified the number of
122 times a vesicle was released over 120 stimuli to determine single-synapse P_r. As has been previously
123 reported, we found that type Is synapses exhibited significant heterogeneity and higher average P_r than
124 type Ib synapses (Fig. 1B, C; (Lu et al. 2016; Newman et al. 2022)). Consistent with their higher P_r,
125 type Is connections contain relatively fewer low-P_r and more high-P_r AZs (Figs. 1D). We next

126 investigated the correlation between P_r and VGCC levels and found that at type Is inputs, single-AZ
127 Cac intensity positively correlates with P_r (Fig. 1E). We also observe a strong positive correlation
128 between VGCC levels and P_r at type Ib inputs to the same muscles (Fig. 1F), consistent with our and
129 others' prior findings (Akbergenova et al. 2018; Gratz et al. 2019; Newman et al. 2022).
130
131 A simple prediction of the observation that VGCC levels correlate highly with P_r at individual AZs of
132 both low- and high-P_r inputs is that Cac levels will be higher at synapses of type Is inputs than type Ib.
133 We analyzed $Cac^{sfGFP-N}$ levels at individual type Ib and Is synapses and found that average Cac levels
134 are the same at type Ib and Is AZs (Fig. 1G, H). Cac levels are also similarly distributed across AZs of
135 the two inputs (Fig. 1I). Together, these findings indicate that the relationship between VGCC levels
136 and P_r differs between the two inputs. Consistently, when we directly compare the best-fit lines for the
137 relationship between Cac levels and P_r at type Ib and Is inputs from our correlative functional imaging
138 data (Fig. 1E, F), we find that the slopes are significantly different (Fig. 1J). Across type Is AZs, a
139 similar range of VGCC levels supports a higher range of release probabilities. Thus, VGCCs can
140 predict P_r within synaptic subtypes, but not between AZs of different synaptic subtypes, providing a
141 framework for understanding seemingly contradictory findings on the role of VGCCs in determining P_r.
142
143 **VGCC clusters are more compact at AZs of high-P_r type Is inputs**
144 Many differences between low-P_r type Ib and high-P_r type Is AZs have been described (Aponte-
145 Santiago and Littleton 2020; Aponte-Santiago et al. 2020; Atwood, Govind, and Wu 1993; He et al.
146 2023; Jetti et al. 2023; Kurdyak et al. 1994; Lu et al. 2016; Medeiros and O'Connor-Giles 2023).
147 Perhaps most notably, type Is AZs experience ~2-fold greater Ca^{2+} influx than type Ib (He et al. 2023;
148 Lu et al. 2016). While this alone could explain the estimated 3-fold greater P_r at type Is AZs and is
149 certainly a key factor, several lines of evidence argue for additional contributors. A recent study using a
150 botulinum transgene to isolate type Ib and Is synapses for electrophysiological analysis found that
151 increasing external [Ca^{2+}] from physiological levels (1.8 mM) to 3 mM or even 6 mM does not result in a
152 3-fold increase in EPSCs or quantal content at type Ib synapses and type Ib synapses continue to

153 facilitate at 3 mM external [Ca^{2+}] (He et al. 2023). Using this approach, they further found that type Ib
154 synapses are more sensitive to the slow Ca^{2+} chelator EGTA, indicating looser VGCC-SV coupling.
155
156 We investigated the spatial distribution of VGCCs at type Ib and Is AZs using 3D dSTORM single-
157 molecule localization microscopy (SMLM). An individual VGCC complex is estimated to be ~10 nm in
158 diameter with the most common immunolabeling techniques adding significantly to their size and
159 creating a linkage error of ~20 nm between the target molecule and fluorescent reporter (Früh et al.
160 2021; Liu, Hoess, and Ries 2022; Thomas 2000). For following VGCC dynamics using single-particle
161 tracking via photoactivation localization microscopy (sptPALM), we recently incorporated mEOS4b
162 (Paez-Segala et al. 2015) at the same N-terminal site we previously used to endogenously tag Cac,
163 achieving a linkage error of less of than 5 nm (Ghelani et al. 2023; Gratz et al. 2019). To gain more
164 flexibility in labeling Cac without adding to the linkage error, we swapped the mEOS tag for a similarly
165 sized HaloTag ($cac^{HaloTag\text{-}N}$). $cac^{HaloTag\text{-}N}$ flies are fully viable, do not display significant defects in
166 synaptic function, and exhibit normal Cac localization at AZs as observed in super-resolution optical
167 reassignment images, where Brp is arranged in rings surrounding puncta of VGCCs (Fig. S1; 2A-C,
168 (Ghelani et al. 2023)). HaloTag, which covalently binds synthetic ligands, is 3.3 nm in diameter (Los et
169 al. 2008; Yazaki et al. 2019), yielding a linkage error well under 5 nm.
170
171 $cac^{HaloTag\text{-}N}$ larvae were stained with JaneliaFluor646 HaloTag ligand (Grimm et al. 2015) and
172 horseradish peroxidase (HRP) to distinguish between type Ib and Is branches and enable simultaneous
173 imaging of the two inputs at a single NMJ. We then used density-based spatial clustering of
174 applications with noise (DBSCAN) analysis to identify Cac clusters at type Ib and Is AZs (Fig. 2D,E;
175 (Ehmann et al. 2014)). We find that the average size of $Cac^{HaloTag\text{-}N}$ clusters is similar at low- and high-
176 P_r AZs (Fig. 2F), with mean diameters of approximately 102 nm and 105 nm, respectively. This is
177 similar to the $Cac^{mEOS4b\text{-}N}$ type Ib cluster size observed by sptPALM imaging (Ghelani et al. 2023). In
178 agreement with our confocal level data, the number of localizations per cluster was similar at low- and
179 high-P_r AZs (Fig. 2G). We then calculated the average Cac density per AZ and found that VGCCs are

180 significantly more densely organized at high-P_r type Is AZs than low-P_r type Ib AZs (Fig. 2H, I). Greater
181 VGCC AZ density at type Is AZs is consistent with a recent SMLM study using antibodies to label Cac,
182 indicating these results are robust to different labeling approaches (Newman et al. 2022). Together,
183 these findings suggest that more compact organization of VGCCs increases their coupling to SVs and
184 contributes to the steeper relationship between VGCC levels and P_r at high-P_r type Is AZs.
185
186 **Differences in Bruchpilot levels and function at low- and high-P_r inputs**
187 To understand how these nanoscale differences in VGCC organization might be established, we
188 investigated the AZ scaffolding protein Brp. Brp/CAST/ELKS family proteins function as central
189 organizers of both VGCCs and SV release sites at developing synapses (Dai et al. 2006; Dong et al.
190 2018; Hallermann et al. 2010; Held, Liu, and Kaeser 2016; Kittel et al. 2006; Liu et al. 2014; McDonald,
191 Fetter, and Shen 2020; Radulovic et al. 2020). Like Cac, Brp is more densely arranged at type Is AZs
192 as measured through SMLM and stimulated emission depletion (STED) imaging studies (He et al.
193 2023; Jetti et al. 2023; Mrestani et al. 2021). We simultaneously imaged type Ib and Is inputs and found
194 lower Brp levels at type Is AZs (Fig. 3A, B). Since Cac levels are similar at AZs of the two inputs, lower
195 Brp levels result in a significantly higher Cac:Brp ratio at type Is synapses, which we hypothesize
196 promotes compact organization of VGCCs (Fig. 3C). In contrast, we and others have previously shown
197 that Brp levels positively correlate with P_r among AZs of low-P_r type Ib inputs (Gratz et al. 2019;
198 Muhammad et al. 2015; Newman et al. 2017; Peled, Newman, and Isacoff 2014; Reddy-Alla et al.
199 2017). Consistently, Brp and Cac levels strongly correlate at type Ib AZs (Gratz et al. 2019) and we
200 observe a similarly strong correlation across individual type Is AZs (Fig. 3D). Thus, like VGCCs, Brp
201 levels contribute in distinct ways to synaptic heterogeneity within vs. between low- and high-P_r inputs,
202 likely due to differences in AZ organization between the two synaptic subtypes.
203
204 We next investigated the requirement for Brp in promoting VGCC accumulation at low- and high-P_r
205 inputs by analyzing $Cac^{sfGFP\text{-}N}$ levels in *brp* null mutants (*brp*$^{-/-}$; Fig. 3E, F). $Cac^{sfGFP\text{-}N}$ levels are
206 diminished at both type Ib and Is AZs, demonstrating a conserved role for Brp in promoting Cac

207 accumulation at both inputs (Fig. 3G). The relative decrease in Cac levels at type Ib AZs is significantly
208 greater than at type Is AZs, indicating a greater requirement for Brp in regulating VGCC levels at low-P_r
209 type Ib synapses (Fig. 3H). This suggests that an additional factor or factors function with or upstream
210 of Brp to establish differences in Brp dependence at low- and high-P_r AZs.
211
212 **Brp differentially regulates VGCC dynamics at low- and high-P_r synapses during presynaptic**
213 **homeostatic potentiation**
214 In response to acute or chronic inhibition of glutamate receptors at NMJs, *Drosophila* motor neurons
215 homeostatically increase neurotransmitter release to maintain synaptic communication (Davis and
216 Muller 2015; Frank 2014; James, Zwiefelhofer, and Frank 2019). Pharmacological inhibition of
217 glutamate receptors with the wasp toxin Philanthotoxin-433 (PhTx) induces acute presynaptic
218 homeostatic potentiation of release (PHP) within minutes (Frank et al. 2006). We and others have
219 demonstrated that acute PHP involves rapid changes in VGCCs and other AZ protein levels at type Ib
220 AZs (Bohme et al. 2019; Gratz et al. 2019; Weyhersmuller et al. 2011). Recent studies have revealed
221 significant differences in the induction of PHP at low- and high-P_r synaptic inputs under different
222 conditions (Genc and Davis 2019; Newman et al. 2017; Sauvola et al. 2021). PhTx induces acute PHP
223 at both type Ib and Is synapses (Genc and Davis 2019), but the molecular changes underlying PHP at
224 high-P_r type Is AZs remain unknown. To compare the dynamic modulation of VGCCs at low- and high-
225 P_r AZs, we treated *cac*$^{sfGFP-N}$ larvae with non-saturating concentrations of PhTx for 10 minutes, then
226 quantified Cac and Brp levels at type Ib and Is AZs (Fig. 4A, B). We observe a significant PhTx-induced
227 increase in Brp and Cac$^{sfGFP-N}$ levels at type Is AZs similar to type Ib (Fig. 4C, D; (Gratz et al. 2019)).
228 Thus, despite their distinct baseline transmission and organizational properties, PhTx-induced
229 potentiation of neurotransmitter release involves the rapid accumulation of VGCCs at both low- and
230 high-P_r AZs.
231
232 At low-P_r type Ib AZs, Brp is a critical regulator of PHP-induced accumulation of proteins associated
233 with SV priming and release, specifically Unc13A and Syntaxin-1A (Bohme et al. 2019). At type Ib AZs,

234 PhTx also induces a Brp-dependent increase in Cac density and decrease in channel mobility (Ghelani
235 et al. 2023). Notably, Brp itself becomes more densely organized during PHP (Ghelani et al. 2023),
236 consistent with its denser organization at high-P_r type Is AZs (Mrestani et al. 2021). Since baseline
237 accumulation of VGCCs depends less on Brp at high-P_r type Is AZs, we investigated the role of Brp in
238 promoting dynamic increases in VGCC levels at type Ib and Is AZs by treating *cac*$^{sfGFP-N}$*; brp*$^{-/-}$ larvae
239 with PhTx followed by quantification of Cac$^{sfGFP-N}$ levels (Fig. 4E, F). We find that PhTx failed to induce
240 accumulation of Cac at either type Ib or Is AZs in *brp*$^{-/-}$ mutants, demonstrating a shared requirement for
241 Brp in regulating VGCC dynamics at both inputs (Fig. 4G). In contrast to no change at type Ib AZs,
242 Cac$^{sfGFP-N}$ levels are significantly decreased at type Is AZs (Fig. 4G), revealing an input-specific role for
243 Brp in maintaining VGCC levels during the dynamic reorganization of AZs. Consistently, Ghelani et al.
244 (2023) found that whereas PhTx induces a decrease in the Cac mobility at wild-type type Ib AZs, in *brp*$^{-}$
245 $^{/-}$ mutants Cac mobility increases (Ghelani et al. 2023). Together, these findings suggest potentiating
246 synapses must coordinate the accumulation of new VGCCs with the stabilization of existing channels,
247 and that meeting this challenge is more dependent upon Brp at high-P_r AZs.
248
249 **Endogenous tagging of VGCC auxiliary subunits reveals distinct synaptic expression patterns**
250 In addition to the pore-forming α subunits, VGCCs comprise auxiliary α2δ and β subunits that regulate
251 forward channel trafficking, membrane insertion, and function (Fig. 5A; (Campiglio and Flucher 2015;
252 Dolphin and Lee 2020; Weiss and Zamponi 2017)). β subunits interact with pore-forming α subunits
253 intracellularly, whereas GPI-anchored α2δ subunits are largely extracellular. Beyond their interaction
254 with α subunits, α2δs have been shown to interact with a growing number of extracellular proteins to
255 promote synaptogenesis (Bauer et al. 2010; Dolphin 2018; Risher et al. 2018). The *Drosophila* genome
256 encodes one synaptic Ca_v2 α subunit (Cac), one β subunit, and three α2δ subunits (Littleton and
257 Ganetzky 2000). Auxiliary subunits are both spatially and temporally regulated and broadly able to
258 interact with α subunits. Thus, the subunit composition of channel complexes is a potential source of
259 significant diversity in both the spatial and functional regulation of VGCCs.
260

261 *Ca-β* encodes the sole *Drosophila* β subunit and has been shown to enhance Ca^{2+} transients in
262 sensory neurons (Kanamori et al. 2013). *Drosophila* α2δ-3, also known as Straightjacket (Stj), has well-
263 characterized roles at the NMJ in promoting Ca^{2+} channel clustering, homeostatic plasticity, and,
264 independently of Cac, synapse formation and organization (Dickman, Kurshan, and Schwarz 2008;
265 Hoover et al. 2019; Kurshan, Oztan, and Schwarz 2009; Ly et al. 2008; Schöpf et al. 2021; Wang et al.
266 2016). While low sequence homology between α2δ subunits within and across species makes 1:1
267 mapping difficult, the remaining two *Drosophila* α2δs map more closely to mammalian α2δ-3 and -4
268 than α2δ-1 and -2. Stolid was recently shown to promote dendritic Cac expression in motor neurons,
269 whereas Ma2d is known to function in muscle where it is broadly expressed (Heinrich and Ryglewski
270 2020; Reuveny et al. 2018). The synaptic localization of endogenous auxiliary subunits with VGCCs
271 remains unknown in *Drosophila*.
272
273 To explore potential differences in VGCC subunit composition at type Ib and Is synapses, we used
274 CRISPR gene editing to incorporate endogenous V5 tags in sequence common to all isoforms of *stj*,
275 *stolid,* and *Ca-β* (Bruckner et al. 2017; Gratz et al. 2014). We inserted V5 after the N-terminal signal
276 peptides of Stj and Stolid and near the C-terminus of Ca-β (see Materials and Methods for details), and
277 confirmed that the incorporation of the peptide tags did not impair neurotransmission (Fig. 5B-E). We
278 investigated the expression of each endogenously tagged subunit in the larval ventral ganglion and
279 found that all subunits are expressed in the synaptic neuropil in a pattern similar to the α subunit Cac
280 (Fig. 5F-H; (Gratz et al. 2019)). Similar to Cac, Ca-$\beta^{V5\text{-}C}$ is highly enriched in the mushroom bodies of
281 the larval brain. We next investigated expression at the larval NMJ where Cac localizes in a single
282 punctum at each AZ and found that only Ca-$\beta^{V5\text{-}C}$ and $Stj^{V5\text{-}N}$ are present (Fig. 5F-H). This aligns with
283 the recent finding that Stolid does not play a role in regulating Ca^{2+} transients at the larval NMJ
284 (Heinrich and Ryglewski 2020). We also observe Ca-$\beta^{V5\text{-}C}$ expression in muscle as expected for the
285 sole *Drosophila* β subunit (Fig. 5F and see Fig. 6C).
286
287 **Stj/α2δ-3 levels are lower at AZs of high-P_r type Is inputs**

288 To investigate Ca-β^{V5-C} and Stj^{V5-N} localization at type Ib and Is AZs, we used super-resolution optical
289 reassignment microscopy. Both subunits localize to AZs labeled with Cac or the CAST/ELKS AZ
290 cytomatrix protein Brp (Fig. 6A, B). We observe Brp rings surrounding puncta of VGCCs including Ca-
291 β^{V5-C} (Fig. 6A). The tight localization of both subunits to central AZ puncta suggests they are associated
292 with α subunits and predicts that Ca-β^{V5-C} and Stj^{V5-N} levels, like Cac, will be similar at the low- and
293 high-P_r synapses. To test this, we simultaneously imaged Ca-β^{V5-C} and Stj^{V5-N} levels at both inputs
294 using confocal microscopy and measured fluorescence intensity (Fig. 6C, D). As predicted, we found
295 that Ca-β^{V5-C} levels are similar at type Ib and Is AZs (Fig. 6E). In contrast, Stj^{V5-N} levels are significantly
296 lower at high-P_r type Is AZs (Fig. 6F). Thus, while Cac and Ca-β are present in similar ratios at AZs of
297 both inputs, surprisingly, the same is not true of Stj/α2δ-3 with high-P_r type Is AZs exhibiting lower
298 levels of Stj. This unexpected finding indicates that α:α2δ-3 stoichiometry is not always 1:1 *in vivo* and
299 differs at low- and high-P_r synapses. This is consistent with studies of mammalian subunits indicating
300 that in contrast to β subunits, α2δ interactions with α subunits may be transient, leading to a pool of
301 VGCCs lacking α2δ (Muller et al. 2010; Voigt et al. 2016). Our results indicate this pool may be present
302 *in vivo* and larger at high-P_r type Is inputs.
303
304 To further investigate the contribution of Stj to synaptic heterogeneity, we analyzed the relationship
305 between Cac and Stj levels at individual AZs of type Is inputs. Stj^{V5-N} and Cac$^{sfGFP-N}$ levels are highly
306 positively correlated at type Is AZs (Fig. 6G). We observe the same relationship between Stj^{V5-N} and
307 Cac$^{sfGFP-N}$ levels at type Ib AZs (Fig. 6H). Because P_r is highly positively correlated with Cac levels
308 within synaptic subtypes, this indicates that Stj levels are also positively correlated with P_r within, but
309 not between, inputs.
310
311 **Stj/α2δ-3 levels are modulated at AZs of both low- and high-P_r inputs during presynaptic**
312 **homeostatic potentiation**
313 α2δ subunits are critical regulators of α subunit forward trafficking. In flies and mammals,
314 overexpression of α2δ subunits increases α subunit abundance, whereas overexpression of the α

315 subunit alone does not (Cao et al. 2004; Cunningham et al. 2022; Hoppa et al. 2012). These findings
316 suggest that α2δ may be dynamically regulated together with Cac during PHP, a prediction we can now
317 test with our endogenously tagged line. Following PhTx exposure, we find that $Stj^{V5\text{-}N}$ is recruited on a
318 rapid timescale to both low- and high-P_r AZs, increasing by a similar percentage at both type Ib and Is
319 AZs (27% and 26%, respectively) as predicted (Fig. 7A-C). Cac levels are similarly increased (33% at
320 type Ib and 30% at type Is; See Fig. 4D), suggesting coordinated regulation. We have previously shown
321 that Cac abundance is also increased in chronic PHP, which is induced by genetic loss of the GluRIIA
322 receptor subunit (Gratz et al. 2019; Li et al. 2018; Petersen et al. 1997). We investigated Stj dynamics
323 in *GluRIIA*$^{-/-}$ null animals and observed elevated $Stj^{V5\text{-}N}$ levels at AZs of both type Ib and Is inputs (18%
324 and 17%, respectively; Fig. 7D-F), indicating similar dynamics during chronic PHP. These data are
325 consistent with the recent finding that in addition to its previously uncovered role in promoting an
326 increase in the readily releasable pool of SVs (Wang et al. 2016), Stj is required for the accumulation of
327 Cac at type Ib AZs during both acute and chronic PHP (Zhang et al. 2023). Thus, the abundance of
328 multiple key AZ proteins distinguishes low- and high-P_r synapses within, but not between, inputs at
329 baseline and during homeostatic plasticity.
330

331 **DISCUSSION**

332 Complex nervous system function depends on communication at synapses with heterogeneous and
333 plastic properties. Paradoxical findings in the field have raised questions about the role of VGCCs in
334 establishing neurotransmitter release properties. Our findings suggest a model in which two broad
335 intersecting mechanisms contribute to synaptic diversity in the nervous system: (1) nanoscale spatial
336 organization and relative molecular content establish distinct average basal release probabilities that
337 differ between inputs and (2) coordinated modulation of VGCC and active zone protein abundance
338 independently tunes P_r among individual synapses of distinct inputs. This model provides a framework
339 for integrating diverse findings in the field and understanding how multiple levels of molecular and
340 organizational diversity can intersect to generate extensive synaptic heterogeneity.
341

342 Investigations at diverse synapses using approaches ranging from cell-attached patch recordings to
343 freeze-fracture immuno-electron microscopy to correlative functional imaging have revealed a strong
344 positive correlation between VGCC number and P_r (Akbergenova et al. 2018; Gratz et al. 2019;
345 Holderith et al. 2012; Miki et al. 2017; Nakamura et al. 2015; Newman et al. 2022; Sheng et al. 2012).
346 This holds true among mature synapses in the hippocampus or immature synapses of the calyx of Held
347 (Holderith et al. 2012; Sheng et al. 2012) and at the developing *Drosophila* NMJ where the differences
348 in P_r and channel number between AZs of a single input also correlate with synapse maturity
349 (Akbergenova et al. 2018; Gratz et al. 2019; Newman et al. 2022). While this conclusion corresponds
350 neatly with the dependence of neurotransmitter release on Ca^{2+} influx, counterintuitively, a disconnect
351 between VGCC and P_r is observed in some studies. Although the number of functional VGCCs
352 positively correlates with P_r among synapses in the immature calyx of Held, the mature calyx has
353 higher P_r yet recruits fewer Ca^{2+} channels (Fedchyshyn and Wang 2005; Sheng et al. 2012; Wang and
354 Augustine 2014). Similarly, in the cerebellum, inhibitory stellate cells form high-P_r synapses with lower
355 VGCC levels than low-P_r synapses formed by excitatory granular cells (Rebola et al. 2019). Adding to
356 these paradoxical examples, we find that VGCC levels positively correlate with P_r among the
357 heterogeneous synapses formed by either low-P_r type Ib or high-P_r type Is motor neurons, but overall
358 VGCC abundance is similar at the two inputs (Figs. 1, 2) despite an ~3-fold difference in P_r (Lu et al.
359 2016; Newman et al. 2017). Accordingly, our correlative functional imaging confirms that the same
360 number of channels can support greater release at these high-P_r AZs (Fig. 1). While two-fold greater
361 Ca^{2+} influx at high-P_r type Is AZs can explain much of this difference (He et al. 2023; Lu et al. 2016),
362 mounting evidence suggests that here and in other systems differences in P_r are separable from Ca^{2+}
363 influx. At distinct inputs formed by CA1 pyramidal neurons, Ca^{2+} influx is greater at high-P_r synapses,
364 but doesn't explain differences in synaptic strength as raising Ca^{2+} entry at low-P_r synapses to high-P_r
365 synapse levels was not sufficient to increase synaptic strength to high-P_r input levels (Aldahabi et al.,
366 2022). Similar findings have been reported at tonic and phasic synapses of the Crayfish NMJ (Msghina,
367 1999).
368

369 The separability of VGCC abundance, Ca^{2+} influx, and P_r appears to be due to molecular and spatial
370 differences between synaptic subtypes. In CA1 pyramidal neurons, differences in Munc-13-dependent
371 SV priming are proposed to establish synapse-specific release properties, possibly due to the presence
372 of distinct isoforms at low- vs. high-P_r connections. In the cerebellum, fewer VGCC are more tightly
373 coupled to SVs at high-P_r stellate synapses (Rebola et al. 2019). More densely organized VGCCs at the
374 mature vs. developing calyx of Held also exhibit greater coupling with SVs (Chen et al. 2015;
375 Fedchyshyn and Wang 2005; Fekete et al. 2019; Nakamura et al. 2015; Sheng et al. 2012). We find
376 that Cac clusters are denser at high-P_r AZs formed by *Drosophila* phasic motor neurons (Fig. 2). Brp,
377 which organizes both VGCCs and SVs, is also more densely organized at type Is synapses (He et al.
378 2023; Jetti et al. 2023; Mrestani et al. 2021), consistent with an overall more compact organization of
379 high-P_r AZs. A straightforward prediction is that a more compact AZ organization will decrease the
380 distance between VGCCs and SVs. Indeed, a recent electrophysiological study using new tools for
381 genetically isolating type Ib and Is inputs demonstrated that neurotransmitter release at denser type Is
382 synapses is less impacted by the slow Ca^{2+} chelator EGTA than type Ib synapses, indicating tighter
383 VGCC-SV coupling (He et al. 2023). Together, these findings suggest that more compact AZs may be a
384 common organizing principle of high-P_r synapses. Consistent with this model, Brp and Unc-13 density
385 increase during PHP when P_r is increased (Dannhauser et al. 2022; Ghelani et al. 2023; Mrestani et al.
386 2021).
387
388 We also observe molecular differences between *Drosophila* motor inputs that may contribute to distinct
389 P_r. Somewhat counterintuitively, high-P_r type Is AZs have lower levels of both Brp and Stj/α2δ-3 (Figs.
390 3, 6). Brp/CAST/ELKS AZ cytomatrix proteins are central regulators of synapse organization across
391 species (Dai et al. 2006; Dong et al. 2018; Hallermann et al. 2010; Held, Liu, and Kaeser 2016; Kittel et
392 al. 2006; Liu et al. 2014; McDonald, Fetter, and Shen 2020; Radulovic et al. 2020). Brp interacts
393 broadly with AZ proteins to promote Cac clustering, organize SVs, and recruit Unc13A, which defines
394 SV release sites (Bohme et al. 2016; Fulterer et al. 2018; Ghelani et al. 2023; Liu et al. 2011). While
395 Brp clearly plays a central role in AZ organization and reorganization, we also find that type Ib and Is

396 synapses have distinct requirements for Brp during synapse formation and homeostatic potentiation
397 (Figs. 3, 4). Synapse-specific roles for Brp are supported by a recent functional imaging study in
398 *Drosophila* (Jetti et al. 2023) and studies of ELKS at mammalian inhibitory and excitatory synapses
399 (Held, Liu, and Kaeser 2016), and suggest additional factors establish neuron-specific differences in
400 Brp dependence. A recent single-cell transcriptomic study of type Ib and Is motor neurons provides an
401 unbiased starting point for identifying candidate regulators of molecular differences at low- and high-P_r
402 AZs (Jetti et al. 2023). Differentially expressed genes encode cytoskeletal and motor-related proteins,
403 regulators of proteostasis, and post-translational modifying enzymes/pathway components – all of
404 which could potentially contribute to establishing the observed molecular and/or spatial differences
405 between type Ib and Is AZs.
406
407 The VGCC complex itself provides an additional potential mechanism for diversifying synaptic function.
408 Both β and α2δ subunits can influence the membrane localization and function of VGCCs (Campiglio
409 and Flucher 2015; Dolphin and Lee 2020; Weiss and Zamponi 2017). In addition to the ability to mix
410 and match subunits, many of the genes encoding VGCC subunits across species are extensively
411 alternatively spliced to generate additional functional diversity (Cingolani et al. 2023; Lipscombe,
412 Andrade, and Allen 2013; Lipscombe and Lopez Soto 2019) – an area of great interest for further
413 investigation at the *Drosophila* NMJ. Because both β and α2δ subunits are generally considered
414 positive regulators of channel trafficking and function, we were surprised to find upon endogenously
415 tagging Stj/α2δ-3 that its levels are lower at high-P_r AZs (Figs. 5, 6). Since AZ levels of α subunit Cac
416 are similar at the two inputs, lower levels of Stj at type Is synapses indicates a difference in α:α2δ-3
417 stoichiometry between low- and high-P_r synaptic subtypes. While some previous studies have observed
418 a tight association between the two subunits, a single-molecule tracking and modeling study of
419 mammalian VGCCs found that α2δ subunits have a relatively low affinity for α subunits and predicted a
420 population of α subunits not associated with an α2δ subunit (Cassidy et al. 2014; Voigt et al. 2016).
421 Consistently, whereas α and β subunits were isolated at near equimolar ratios following affinity
422 purification of Ca_v2 channels, molar levels of α2δ were a surprising 90% lower (Muller et al. 2010). Our

423 findings suggest there may be a pool of VGCCs lacking an α2δ subunit at endogenous synapses, and
424 further suggest that this pool is specific to or enriched at high-P_r type Is AZs. Stj is both required
425 (Dickman, Kurshan, and Schwarz 2008; Kurshan, Oztan, and Schwarz 2009; Ly et al. 2008) and rate
426 limiting (Cunningham et al. 2022) for Cac accumulation at AZs. Stj does not appear to function in the
427 stabilization of channels at the AZ membrane, but rather at an upstream step in the progression from
428 ER to plasma membrane (Cunningham et al. 2022), so complexes may not need to be maintained.
429 Tools for following Stj dynamics in developing neurons will help clarify its precise role in Cac delivery at
430 type Ib and Is AZs.
431
432 How might a higher α:α2δ-3 ratio result in higher P_r? One possibility involves α2δ-3 interactions with
433 cell adhesion molecules. In mammals, α-Neurexin specifically inhibits Ca^{2+} currents in $Ca_v2.2$ channels
434 containing α2δ-3 (Tong et al. 2017), which, if similar at the *Drosophila* NMJ, could result in greater
435 inhibition of channel function at type Ib AZs and contribute to the observed difference in Ca^{2+} influx.
436 Loss of *Drosophila* Neurexin reduces neurotransmitter release at the NMJ, but it also leads to reduced
437 synaptogenesis so whether this is a direct effect remains unknown (Li et al. 2007). Another possibility is
438 that Stj isoforms with different functions are differentially expressed at type Ib and Is AZs. A recent
439 transcriptomic study observed no significant differences in mRNA splice isoforms, but transcript levels
440 do not always reflect protein levels (Jetti et al. 2023). Notably, we find that among synapses of either
441 low- or high-P_r AZs, Stj levels correlate with P_r and Stj levels are increased across AZs of both inputs
442 during acute and chronic PHP (Fig. 7). Cac and Stj levels increase by similar amounts at the two inputs,
443 suggesting the difference in stoichiometry is maintained following homeostatic potentiation. α2δ-3 is an
444 important drug target for treating epilepsy, neuropathic pain, and anxiety, so understanding its cell-
445 specific roles and how α:α2δ-3 stoichiometry impacts channel function and contributes to synaptic
446 diversity is of great interest.

447 **MATERIALS AND METHODS**

448 *Drosophila genetics and gene editing*

449 The following fly lines used in this study were obtained from the Bloomington Drosophila Stock Center
450 (BDSC, NIH P40OD018537): w^{1118} (RRID:BDSC_5905), *vasa-Cas9* (RRID:BDSC_51324), piggyBac
451 transposase (RRID:BDSC_8283), and $Df(2R)brp^{6.1}$ (Gratz et al. 2014; Horn et al. 2003). brp^{69} and
452 $GluRIIA^{sp16}$ ($GluRIIA^{-/-}$) alleles were generously provided by Stephan Sigrist (Freie Universität Berlin;
453 (Fouquet et al. 2009; Kittel et al. 2006)) and Aaron DiAntonio (Petersen et al. 1997) respectively. *brp*
454 loss-of-function experiments were performed in $brp^{69}/Df(2R)brp^{6.1}$. *Drosophila melanogaster* stocks
455 were raised on molasses food (Lab Express, Type R) in a 25°C incubator with controlled humidity and
456 12h light/dark cycle. Endogenously tagged *cac*, *Ca-β*, *stolid*, and *straightjacket* (*stj*) alleles were
457 generated using our piggyBac-based CRISPR approach as previously detailed
458 (flyCRISPR.molbio.wisc.edu; (Bruckner et al. 2017; Gratz et al. 2019)). We used FlyBase (release
459 FB2024_01) to obtain genomic sequences (doi.org/10.1093/genetics/iyad211). Td-Tomato and Halo
460 tags were incorporated at the N-terminus of Cac, where we have previously incorporated fluorescent
461 tags (Ghelani et al. 2023; Gratz et al. 2019). V5 tags were incorporated at the N-terminus of Stj and
462 Stolid after their signal peptide sequences, immediately after Asparagine 34 of Stj and after Isoleucine
463 34 of Stolid. For Ca-β, V5 was inserted immediately after Proline 446 of isoform Ca-β-PN. All
464 endogenously tagged lines are fully viable in homozygous males and females and were molecularly
465 confirmed by Sanger sequencing.

466

467 *Immunostaining*

468 All antibodies used, associated fixation methods, and incubation times can be found in Table S2. Male
469 wandering third-instar larvae were dissected in ice-cold saline and fixed either for 6 minutes at room
470 temperature with Bouin's fixative, 5 minutes on ice with 100% methanol, or 30 minutes at room
471 temperature (RT) in 4% PFA. Dissections were permeabilized with PTX (PBS with 0.1% Triton-X 100)
472 and blocked for 1 hour at RT using 5% goat serum and 1% bovine serum albumin. Stained larvae were
473 mounted in Vectashield (Vector Laboratories, #H-1000) under Fisherbrand coverglass (Fisher

474 Scientific, #12541B) for confocal microscopy, with Prolong glass mounting medium (ThermoFisher
475 Scientific, #P36980) under Zeiss High Performance Coverglass (Zeiss, #474030-9000-000) for super-
476 resolution optical reassignment microscopy, or buffer (see STORM imaging and analysis section) under
477 Zeiss coverglass with edges sealed using vacuum grease for STORM microscopy.
478
479 *Ca^{2+} imaging and analysis*
480 Functional imaging was performed on a Nikon A1R resonant scanning confocal mounted on a FN1
481 microscope using a Nikon Apo LWD 25x 1.1 NA objective and a Mad City Labs piezo drive nosepiece.
482 Dissections and data collection were performed as previously described in Gratz et al., 2019. Briefly,
483 *$cac^{Td\text{-}Tomato\text{-}N}$*; *Mhc-GCaMP6f* male 3rd instar larvae were dissected in HL3 containing 0.2mM Ca^{2+} and
484 25mM Mg^{2+} with motor axons severed and the larval brain removed. Larval filets were placed in HL3
485 containing 1.5mM Ca^{2+} and 25mM Mg^{2+} for recording. Nerves were suctioned into 1.5mm pipettes and
486 stimulus amplitude was adjusted to recruit both type Ib and Is inputs. Motor terminals from segments
487 A2-4 at NMJ 6/7 were imaged for $Cac^{Td\text{-}Tomato\text{-}N}$ levels first using a galvanometer scanner, then a
488 resonant scanner to collect GCaMP6f events in a single focal plane continuously for 120 stimulations at
489 a 0.2 Hz stimulation frequency.
490
491 Z-stacks and movies were loaded into Nikon Elements Software (NIS) where movies were motion
492 corrected, background subtracted, and denoised. Change in fluorescence (ΔF) movies were then
493 created by subtracting the average of the previous 10 frames from each frame. A substack of only
494 stimulation frames was further processed using a gaussian filter followed by the Bright Spots detection
495 module in the Nikon GA3 software to identify the location of each postsynaptic event. $Cac^{Td\text{-}Tomato\text{-}N}$
496 fluorescence intensity levels and coordinate locations were measured for 531 AZs for type Ib and 365
497 AZs for type Is terminals across 6 animals. X-Y coordinate positions of fluorescent signals from
498 GCaMP6f postsynaptic events were aligned to $Cac^{Td\text{-}Tomato\text{-}N}$ puncta locations and each post synaptic
499 event assigned to a Cac punctum using nearest neighbor analysis. Postsynaptic events that did not
500 map within 960 nm of a $Cac^{Td\text{-}Tomato\text{-}N}$ punctum were discarded from the analysis. Pearson's correlation

501 was used to determine the correlation between P_r and Cac levels normalized to average to account for
502 variability between imaging sessions. Cac intensity-P_r heat maps were generated using Python
503 matplotlib and seaborn plotting packages.
504
505 *STORM imaging and analysis*
506 STORM imaging was performed on a Nikon Eclipse Ti2 3D NSTORM with an Andor iXon Ultra camera,
507 Nikon LUN-F 405/488/640 nm lasers, and a Nikon 100x 1.49 NA objective. STORM buffer (10mM MEA
508 (pH 8.0), 3 U/mL pyranose oxidase, and 90 U/mL catalase, 10% (w/v) glucose, 10 mM sodium chloride,
509 and 50 mM Tris hydrochloride) was made fresh each imaging day and pH adjusted to between 7.0-8.0
510 using acetic acid. *cac*$^{HaloTag\text{-}N}$ NMJs were labeled as detailed in Table S2 and immediately imaged for
511 HRP in 488 channel to identify type Ib and Is terminals. Cac$^{HaloTag\text{-}N}$ was then imaged using the 640 nm
512 laser line at 33 Hz for 5000 frames. 405 nm laser power was gradually increased over the course of
513 imaging to compensate for run-down of blinking rates. A back aperture camera was used to ensure
514 beam focus and position for each imaging session to ensure high signal to noise. Data were binned
515 with a CCD minimum threshold of 100 and drift correction was applied using the NIS Software STORM
516 package. ROIs of single boutons were drawn in NIS using HRP in the 488 nm channel followed by a
517 DBSCAN analysis with criteria of 10 molecules within 50 nm to determine clusters. Positional
518 coordinates of localizations within clusters from DBSCAN were exported from NIS and run through a
519 Python script published with this manuscript. Using the implementation developed in Mrestani et al.,
520 2021 as a starting point, we wrote custom code to use the alpha shapes component of the CGAL
521 package (https://www.cgal.org), via a python wrapper (https://anaconda.org/conda-forge/cgal), to
522 measure the area of Ca^{2+} channel clusters, the number of localizations, and calculate cluster density.
523 To achieve an average lateral localization accuracy of ~30 nm, all localizations with >50 nm localization
524 accuracy were removed prior to analysis. Using this custom code, Cac$^{HaloTag\text{-}N}$ area was analyzed using
525 an alpha value of 0.015, which controls the complexity of cluster boundaries (not restricted to be
526 convex).
527

528 *Confocal imaging and analysis*

529 For quantitative AZ analysis of larval NMJs, dissections stained in the same dish were imaged on a
530 Nikon Eclipse Ni A1R+ confocal microscope using an Apo TIRF 60x 1.49 NA oil-immersion objective for
531 larval NMJs. NMJs containing both type Is and type Ib branches from muscles 6/7 in segments A2-4
532 were collected. ROIs were drawn using HRP staining to differentiate between type Ib and Is branches.
533 To analyze individual AZs, Nikon Elements GA3 Software was used to process images with Gaussian
534 and rolling ball filters and measure fluorescence intensity levels at individual puncta identified by the
535 Bright Spots module. When experimental design allowed, Brp fluorescence signal was used to create a
536 binary mask to aid in the identification of AZ ROIs for analysis. Otherwise, binary masks were created
537 based on the fluorescence signal of the channel analyzed. Confocal fluorescence intensity level data
538 are reported as the sum fluorescence intensity per AZ averaged over individual NMJs. For Fig. 5,
539 larvae were stained separately and imaged using a Nikon Plan-Apo 20x 0.75 NA objective (ventral
540 ganglia) or Apo TIRF 60x 1.49 NA oil-immersion objective (NMJs).

541

542 Super-resolution optical reassignment images were obtained on a Nikon CSU-W1 SoRa (Spinning Disk
543 Super Resolution by Optical Pixel Reassignment) with a Photometrics Prime BSI sCMOS camera and a
544 60x 1.49 NA oil-immersion objective. Images were acquired using Nikon NIS and deconvolved using
545 Richardson-Lucy deconvolution with 15-20 iterations.

546

547 *Electrophysiology*

548 Current-clamp recordings were performed as previously described (Bruckner et al. 2017). Male third-
549 instar larvae were dissected in HL3 (70 mM NaCl, 5 mM KCl, 15 mM MgCl2, 10 mM NaHCO3, 115 mM
550 sucrose, 5 mM trehalose, 5 mM HEPES, pH 7.2) with 0.25 mM Ca^{2+}. Recordings were performed in
551 HL3 at the external Ca^{2+} concentration indicated. Sharp borosilicate electrodes filled with 3 M KCl were
552 used to record from muscle 6 of abdominal segments A3 and A4. Recordings were conducted on a
553 Nikon FN1 microscope using a 40x 0.80 NA water-dipping objective and acquired using an Axoclamp
554 900A amplifier, Digidata 1550B acquisition system, and pClamp 11.0.3 software (Molecular Devices).

555

556 For each cell with an initial resting potential between −60 and −80 mV and input resistance ≥5 MΩ,
557 mean miniature excitatory junctional potentials (mEJPs) were collected for 1 minute in the absence of
558 stimulation and analyzed using Mini Analysis (Synaptosoft). EJPs were generated by applying a
559 stimulus to severed segmental nerves at a frequency of 0.2 Hz using an isolated pulse stimulator 2100
560 (A-M Systems). Stimulus amplitude was adjusted to consistently elicit compound responses from both
561 type Ib and Is motor neurons. At least 25 consecutive EJPs were recorded for each cell and analyzed in
562 pClamp to obtain mean amplitude. Quantal content was calculated for each recording as mean EJP
563 amplitude divided by mean mEJP amplitude.

564

565 *Acute homeostatic challenge*

566 Acute PHP was induced by incubating semi-intact preparations in 20 μM Philanthotoxin-433 (Fig. 4:
567 PhTx; Santa Cruz, sc-255421, Lot B1417 and Fig. 7: PhTx; Sigma Aldrich, P207-2, Lot MKCK7405)
568 diluted in HL3 containing 0.4 mM Ca^{2+} for 10 minutes at room temperature (Frank et al. 2006). Control
569 preparations were given a mock treatment. Following control and experimental treatment, dissections
570 were completed, fixed in 4% PFA for 30 minutes ($cac^{sfGFP\text{-}N}$) or 100% ice-cold methanol on ice for 5
571 minutes ($stj^{V5\text{-}N}$), and stained in the same dish. Analyses of fluorescent intensity levels were performed
572 as previously described in the *Confocal imaging and analysis section.*

573

574 *Experimental design and statistical analysis*

575 Statistical analyses were conducted in GraphPad Prism 9. Normality was determined by the
576 D'Agostino–Pearson omnibus test. Comparisons of normally distributed data were conducted by
577 Student's *t* test (with Welch's correction in the case of unequal variance) for single comparisons and
578 ANOVA followed by Tukey's test for multiple comparisons. For non-normally distributed data, the
579 Mann–Whitney *U* test and Kruskal-Wallis test followed by Dunn's multiple comparisons tests were used
580 for single and multiple comparisons, respectively. Paired analysis of non-normally distributed data was
581 conducted using Wilcoxon's matched-pairs signed rank test. One-dimensional Pearson correlation

582 coefficients (*r*) were used to compare intensity levels and neurotransmitter release probability.
583 ANCOVA test was performed on all regression lines to determine if slopes were significantly different.
584 Reported values are mean ± SEM. Sample size, statistical test, and *p* values for each comparison are
585 reported in Table S1.
586

587 **ACKNOWLEDGEMENTS**

588 We thank the Developmental Studies Hybridoma Bank, the Bloomington *Drosophila* Stock Center (NIH
589 P40OD018537), Flybase (Öztürk-Çolak et al. 2024), Ehud Isacoff (UC Berkeley), and Stephan Sigrist
590 (Freie Universität Berlin) for providing antibodies and fly stocks. The Nikon SoRa/STORM microscope
591 was generously provided by The Neurobiology of Cells and Circuits/Center for Translational
592 Neuroscience Microscopy Committee, Carney Institute for Brain Science. We are grateful to Joel Hirsch
593 (Tel Aviv University) for consultations on tagging Ca-β, Nicholas Deakin (Nikon) for guidance on
594 STORM imaging, the Heckmann lab (University of Würzburg) for guidance on STORM image analysis
595 pipelines, Matthew Knoeppel for help generating CRISPR alleles, and Liana Lewis for her assistance
596 with image analysis. We thank Rajan Thakur and the members of the O'Connor-Giles lab for thoughtful
597 discussions and comments on the manuscript. This work was supported by grants from the National
598 Institute of Neurological Disorders and Stroke, National Institutes of Health to K.M.O.G (R01NS078179)
599 and Audrey Medeiros (F31NS122424), Brown Neuroscience Graduate Program training grant T32
600 MH020068, and funds from the Brown University Carney Institute for Brain Science.

601 **REFERENCES**

602 Akbergenova, Yulia, Karen L. Cunningham, Yao V. Zhang, Shirley Weiss, and J. Troy Littleton. 2018.
603 'Characterization of developmental and molecular factors underlying release heterogeneity at
604 Drosophila synapses', *eLife*, 7.

605 Aldahabi, M., F. Balint, N. Holderith, A. Lorincz, M. Reva, and Z. Nusser. 2022. 'Different priming states
606 of synaptic vesicles underlie distinct release probabilities at hippocampal excitatory synapses', *Neuron*,
607 110: 4144-61 e7.

608 Aponte-Santiago, N. A., and J. T. Littleton. 2020. 'Synaptic Properties and Plasticity Mechanisms of
609 Invertebrate Tonic and Phasic Neurons', *Front Physiol*, 11: 611982.

610 Aponte-Santiago, N. A., K. G. Ormerod, Y. Akbergenova, and J. T. Littleton. 2020. 'Synaptic Plasticity
611 Induced by Differential Manipulation of Tonic and Phasic Motoneurons in Drosophila', *J Neurosci*, 40:
612 6270-88.

613 Ariel, P., M. B. Hoppa, and T. A. Ryan. 2012. 'Intrinsic variability in Pv, RRP size, Ca(2+) channel
614 repertoire, and presynaptic potentiation in individual synaptic boutons', *Front Synaptic Neurosci*, 4: 9.

615 Atwood, H. L., C. K. Govind, and C.-F. Wu. 1993. 'Differential ultrastructure of synaptic terminals on
616 ventral longitudinal abdominal muscles in Drosophila larvae', *Journal of Neurobiology*, 24: 1008-24.

617 Atwood, H. L., and S. Karunanithi. 2002. 'Diversification of synaptic strength: presynaptic elements', *Nat*
618 *Rev Neurosci*, 3: 497-516.

619 Bauer, C. S., A. Tran-Van-Minh, I. Kadurin, and A. C. Dolphin. 2010. 'A new look at calcium channel
620 alpha2delta subunits', *Curr Opin Neurobiol*, 20: 563-71.

621 Bohme, M. A., C. Beis, S. Reddy-Alla, E. Reynolds, M. M. Mampell, A. T. Grasskamp, J. Lutzkendorf,
622 D. D. Bergeron, J. H. Driller, H. Babikir, F. Gottfert, I. M. Robinson, C. J. O'Kane, S. W. Hell, M. C.
623 Wahl, U. Stelzl, B. Loll, A. M. Walter, and S. J. Sigrist. 2016. 'Active zone scaffolds differentially
624 accumulate Unc13 isoforms to tune Ca(2+) channel-vesicle coupling', *Nat Neurosci*, 19: 1311-20.

625 Bohme, M. A., A. W. McCarthy, A. T. Grasskamp, C. B. Beuschel, P. Goel, M. Jusyte, D. Laber, S.
626 Huang, U. Rey, A. G. Petzoldt, M. Lehmann, F. Gottfert, P. Haghighi, S. W. Hell, D. Owald, D.
627 Dickman, S. J. Sigrist, and A. M. Walter. 2019. 'Rapid active zone remodeling consolidates presynaptic
628 potentiation', *Nat Commun*, 10: 1085.

629 Branco, T., and K. Staras. 2009. 'The probability of neurotransmitter release: variability and feedback
630 control at single synapses', *Nat Rev Neurosci*, 10: 373-83.

631 Bruckner, J. J., H. Zhan, S. J. Gratz, M. Rao, F. Ukken, G. Zilberg, and K. M. O'Connor-Giles. 2017.
632 'Fife organizes synaptic vesicles and calcium channels for high-probability neurotransmitter release', *J*
633 *Cell Biol*, 216: 231-46.

634 Campiglio, Marta, and Bernhard E. Flucher. 2015. 'The Role of Auxiliary Subunits for the Functional
635 Diversity of Voltage-Gated Calcium Channels', *Journal of Cellular Physiology*, 230: 2019-31.

636 Cao, Yu-Qing, Erika S. Piedras-Rentería, Geoffrey B. Smith, Gong Chen, Nobutoshi C. Harata, and
637 Richard W. Tsien. 2004. 'Presynaptic Ca²⁺ Channels Compete for Channel Type-
638 Preferring Slots in Altered Neurotransmission Arising from Ca²⁺ Channelopathy', *Neuron*,
639 43: 387-400.

Cassidy, J. S., L. Ferron, I. Kadurin, W. S. Pratt, and A. C. Dolphin. 2014. 'Functional exofacially tagged N-type calcium channels elucidate the interaction with auxiliary alpha2delta-1 subunits', *Proc Natl Acad Sci U S A*, 111: 8979-84.

Chen, Z., B. Das, Y. Nakamura, D. A. DiGregorio, and S. M. Young, Jr. 2015. 'Ca2+ channel to synaptic vesicle distance accounts for the readily releasable pool kinetics at a functionally mature auditory synapse', *J Neurosci*, 35: 2083-100.

Cingolani, Lorenzo A., Agnes Thalhammer, Fanny Jaudon, Jessica Muià, and Gabriele Baj. 2023. 'Nanoscale organization of CaV2.1 splice isoforms at presynaptic terminals: implications for synaptic vesicle release and synaptic facilitation', 404: 931-37.

Cunningham, K. L., C. W. Sauvola, S. Tavana, and J. T. Littleton. 2022. 'Regulation of presynaptic Ca(2+) channel abundance at active zones through a balance of delivery and turnover', *eLife*, 11.

Dai, Y., H. Taru, S. L. Deken, B. Grill, B. Ackley, M. L. Nonet, and Y. Jin. 2006. 'SYD-2 Liprin-alpha organizes presynaptic active zone formation through ELKS', *Nat Neurosci*, 9: 1479-87.

Dannhauser, S., A. Mrestani, F. Gundelach, M. Pauli, F. Komma, P. Kollmannsberger, M. Sauer, M. Heckmann, and M. M. Paul. 2022. 'Endogenous tagging of Unc-13 reveals nanoscale reorganization at active zones during presynaptic homeostatic potentiation', *Front Cell Neurosci*, 16: 1074304.

Davis, G. W., and M. Muller. 2015. 'Homeostatic control of presynaptic neurotransmitter release', *Annu Rev Physiol*, 77: 251-70.

Dickman, D. K., P. T. Kurshan, and T. L. Schwarz. 2008. 'Mutations in a Drosophila alpha2delta voltage-gated calcium channel subunit reveal a crucial synaptic function', *J Neurosci*, 28: 31-8.

Dolphin, A. C. 2018. 'Voltage-gated calcium channel alpha (2)delta subunits: an assessment of proposed novel roles', *F1000Res*, 7.

Dolphin, A. C., and A. Lee. 2020. 'Presynaptic calcium channels: specialized control of synaptic neurotransmitter release', *Nat Rev Neurosci*, 21: 213-29.

Dong, W., T. Radulovic, R. O. Goral, C. Thomas, M. Suarez Montesinos, D. Guerrero-Given, A. Hagiwara, T. Putzke, Y. Hida, M. Abe, K. Sakimura, N. Kamasawa, T. Ohtsuka, and S. M. Young, Jr. 2018. 'CAST/ELKS Proteins Control Voltage-Gated Ca(2+) Channel Density and Synaptic Release Probability at a Mammalian Central Synapse', *Cell Rep*, 24: 284-93 e6.

Eggermann, E., I. Bucurenciu, S. P. Goswami, and P. Jonas. 2011. 'Nanodomain coupling between Ca(2)(+) channels and sensors of exocytosis at fast mammalian synapses', *Nat Rev Neurosci*, 13: 7-21.

Ehmann, Nadine, Sebastian Van De Linde, Amit Alon, Dmitrij Ljaschenko, Xi Zhen Keung, Thorge Holm, Annika Rings, Aaron Diantonio, Stefan Hallermann, Uri Ashery, Manfred Heckmann, Markus Sauer, and Robert J. Kittel. 2014. 'Quantitative super-resolution imaging of Bruchpilot distinguishes active zone states', *Nature Communications*, 5.

Fedchyshyn, M. J., and L. Y. Wang. 2005. 'Developmental transformation of the release modality at the calyx of Held synapse', *J Neurosci*, 25: 4131-40.

Fekete, A., Y. Nakamura, Y. M. Yang, S. Herlitze, M. D. Mark, D. A. DiGregorio, and L. Y. Wang. 2019. 'Underpinning heterogeneity in synaptic transmission by presynaptic ensembles of distinct morphological modules', *Nat Commun*, 10: 826.

680 Fouquet, W., D. Owald, C. Wichmann, S. Mertel, H. Depner, M. Dyba, S. Hallermann, R. J. Kittel, S.
681 Eimer, and S. J. Sigrist. 2009. 'Maturation of active zone assembly by Drosophila Bruchpilot', *J Cell*
682 *Biol*, 186: 129-45.

683 Frank, C. A. 2014. 'Homeostatic plasticity at the Drosophila neuromuscular junction',
684 *Neuropharmacology*, 78: 63-74.

685 Frank, C. A., M. J. Kennedy, C. P. Goold, K. W. Marek, and G. W. Davis. 2006. 'Mechanisms
686 underlying the rapid induction and sustained expression of synaptic homeostasis', *Neuron*, 52: 663-77.

687 Früh, Susanna M., Ulf Matti, Philipp R. Spycher, Marina Rubini, Sebastian Lickert, Thomas
688 Schlichthaerle, Ralf Jungmann, Viola Vogel, Jonas Ries, and Ingmar Schoen. 2021. 'Site-Specifically-
689 Labeled Antibodies for Super-Resolution Microscopy Reveal In Situ Linkage Errors', *ACS Nano*, 15:
690 12161-70.

691 Fulterer, A., T. F. M. Andlauer, A. Ender, M. Maglione, K. Eyring, J. Woitkuhn, M. Lehmann, T.
692 Matkovic-Rachid, J. R. P. Geiger, A. M. Walter, K. I. Nagel, and S. J. Sigrist. 2018. 'Active Zone
693 Scaffold Protein Ratios Tune Functional Diversity across Brain Synapses', *Cell Rep*, 23: 1259-74.

694 Genc, O., and G. W. Davis. 2019. 'Target-wide Induction and Synapse Type-Specific Robustness of
695 Presynaptic Homeostasis', *Curr Biol*, 29: 3863-73 e2.

696 Ghelani, Tina, Marc Escher, Ulrich Thomas, Klara Esch, Janine Lützkendorf, Harald Depner, Marta
697 Maglione, Pierre Parutto, Scott Gratz, Tanja Matkovic-Rachid, Stefanie Ryglewski, Alexander M.
698 Walter, David Holcman, Kate O‘Connor Giles, Martin Heine, and Stephan J. Sigrist. 2023. 'Interactive
699 nanocluster compaction of the ELKS scaffold and Cacophony Ca²⁺ channels drives
700 sustained active zone potentiation', *Science Advances*, 9: eade7804.

701 Gratz, S. J., F. P. Ukken, C. D. Rubinstein, G. Thiede, L. K. Donohue, A. M. Cummings, and K. M.
702 O'Connor-Giles. 2014. 'Highly specific and efficient CRISPR/Cas9-catalyzed homology-directed repair
703 in Drosophila', *Genetics*, 196: 961-71.

704 Gratz, Scott J., Pragya Goel, Joseph J. Bruckner, Roberto X. Hernandez, Karam Khateeb, Gregory T.
705 Macleod, Dion Dickman, and Kate M. O'Connor-Giles. 2019. 'Endogenous tagging reveals differential
706 regulation of Ca²⁺ channels at single AZs during presynaptic homeostatic potentiation
707 and depression', *The Journal of Neuroscience*: 3068-18.

708 Grimm, J. B., B. P. English, J. Chen, J. P. Slaughter, Z. Zhang, A. Revyakin, R. Patel, J. J. Macklin, D.
709 Normanno, R. H. Singer, T. Lionnet, and L. D. Lavis. 2015. 'A general method to improve fluorophores
710 for live-cell and single-molecule microscopy', *Nat Methods*, 12: 244-50, 3 p following 50.

711 Guerrero, G., D. F. Reiff, G. Agarwal, R. W. Ball, A. Borst, C. S. Goodman, and E. Y. Isacoff. 2005.
712 'Heterogeneity in synaptic transmission along a Drosophila larval motor axon', *Nat Neurosci*, 8: 1188-
713 96.

714 Hallermann, S., R. J. Kittel, C. Wichmann, A. Weyhersmuller, W. Fouquet, S. Mertel, D. Owald, S.
715 Eimer, H. Depner, M. Schwarzel, S. J. Sigrist, and M. Heckmann. 2010. 'Naked dense bodies provoke
716 depression', *J Neurosci*, 30: 14340-5.

717 Hatt, H., and D. O. Smith. 1976. 'Non-uniform probabilities of quantal release at the crayfish
718 neuromuscular junction', *J Physiol*, 259: 395-404.

He, K., Y. Han, X. Li, R. X. Hernandez, D. V. Riboul, T. Feghhi, K. A. Justs, O. Mahneva, S. Perry, G. T. Macleod, and D. Dickman. 2023. 'Physiologic and Nanoscale Distinctions Define Glutamatergic Synapses in Tonic vs Phasic Neurons', *J Neurosci*, 43: 4598-611.

Heinrich, Laurin, and Stefanie Ryglewski. 2020. 'Different functions of two putative Drosophila α2δ subunits in the same identified motoneurons', *Scientific Reports*, 10: 13670.

Held, R. G., C. Liu, and P. S. Kaeser. 2016. 'ELKS controls the pool of readily releasable vesicles at excitatory synapses through its N-terminal coiled-coil domains', *eLife*, 5.

Holderith, Noemi, Andrea Lorincz, Gergely Katona, Balázs Rózsa, Akos Kulik, Masahiko Watanabe, and Zoltan Nusser. 2012. 'Release probability of hippocampal glutamatergic terminals scales with the size of the active zone', *Nat Neurosci*, 15: 988-97.

Hoover, K. M., S. J. Gratz, N. Qi, K. A. Herrmann, Y. Liu, J. J. Perry-Richardson, P. J. Vanderzalm, K. M. O'Connor-Giles, and H. T. Broihier. 2019. 'The calcium channel subunit alpha(2)delta-3 organizes synapses via an activity-dependent and autocrine BMP signaling pathway', *Nat Commun*, 10: 5575.

Hoppa, Michael B., Beatrice Lana, Wojciech Margas, Annette C. Dolphin, and Timothy A. Ryan. 2012. 'α2δ expression sets presynaptic calcium channel abundance and release probability', *Nature*, 486: 122-25.

Horn, C., N. Offen, S. Nystedt, U. Hacker, and E. A. Wimmer. 2003. 'piggyBac-based insertional mutagenesis and enhancer detection as a tool for functional insect genomics', *Genetics*, 163: 647-61.

James, T. D., D. J. Zwiefelhofer, and C. A. Frank. 2019. 'Maintenance of homeostatic plasticity at the Drosophila neuromuscular synapse requires continuous IP(3)-directed signaling', *eLife*, 8.

Jetti, Suresh K., Andrés B. Crane, Yulia Akbergenova, Nicole A. Aponte-Santiago, Karen L. Cunningham, Charles A. Whittaker, and J. Troy Littleton. 2023. 'Molecular logic of synaptic diversity between Drosophila tonic and phasic motoneurons', *Neuron*, 111: 3554-69.e7.

Kanamori, T., M. I. Kanai, Y. Dairyo, K. Yasunaga, R. K. Morikawa, and K. Emoto. 2013. 'Compartmentalized calcium transients trigger dendrite pruning in Drosophila sensory neurons', *Science*, 340: 1475-8.

Kawasaki, F., R. Felling, and R. W. Ordway. 2000. 'A temperature-sensitive paralytic mutant defines a primary synaptic calcium channel in Drosophila', *J Neurosci*, 20: 4885-9.

Kittel, Robert J., Carolin Wichmann, Tobias M. Rasse, Wernher Fouquet, Manuela Schmidt, Andreas Schmid, Dhananjay A. Wagh, Christian Pawlu, Robert R. Kellner, Katrin I. Willig, Stefan W. Hell, Erich Buchner, Manfred Heckmann, and Stephan J. Sigrist. 2006. 'Bruchpilot Promotes Active Zone Assembly, Ca²⁺ Channel Clustering, and Vesicle Release', *Science*, 312: 1051-54.

Kurdyak, P., H. L. Atwood, B. A. Stewart, and C. F. Wu. 1994. 'Differential physiology and morphology of motor axons to ventral longitudinal muscles in larval Drosophila', *J Comp Neurol*, 350: 463-72.

Kurshan, P. T., A. Oztan, and T. L. Schwarz. 2009. 'Presynaptic alpha2delta-3 is required for synaptic morphogenesis independent of its Ca2+-channel functions', *Nat Neurosci*, 12: 1415-23.

Laghaei, R., J. Ma, T. B. Tarr, A. E. Homan, L. Kelly, M. S. Tilvawala, B. S. Vuocolo, H. P. Rajasekaran, S. D. Meriney, and M. Dittrich. 2018. 'Transmitter release site organization can predict synaptic function at the neuromuscular junction', *J Neurophysiol*, 119: 1340-55.

Li, Jingjun, James Ashley, Vivian Budnik, and Manzoor A. Bhat. 2007. 'Crucial Role of Drosophila Neurexin in Proper Active Zone Apposition to Postsynaptic Densities, Synaptic Growth, and Synaptic Transmission', *Neuron*, 55: 741-55.

Li, Xiling, Pragya Goel, Joyce Wondolowski, Jeremy Paluch, and Dion Dickman. 2018. 'A Glutamate Homeostat Controls the Presynaptic Inhibition of Neurotransmitter Release', *Cell Reports*, 23: 1716-27.

Lipscombe, D., A. Andrade, and S. E. Allen. 2013. 'Alternative splicing: functional diversity among voltage-gated calcium channels and behavioral consequences', *Biochim Biophys Acta*, 1828: 1522-9.

Lipscombe, D., and E. J. Lopez Soto. 2019. 'Alternative splicing of neuronal genes: new mechanisms and new therapies', *Curr Opin Neurobiol*, 57: 26-31.

Littleton, J. Troy, and Barry Ganetzky. 2000. 'Ion Channels and Synaptic Organization', *Neuron*, 26: 35-43.

Liu, C., L. S. Bickford, R. G. Held, H. Nyitrai, T. C. Sudhof, and P. S. Kaeser. 2014. 'The active zone protein family ELKS supports Ca2+ influx at nerve terminals of inhibitory hippocampal neurons', *J Neurosci*, 34: 12289-303.

Liu, K. S., M. Siebert, S. Mertel, E. Knoche, S. Wegener, C. Wichmann, T. Matkovic, K. Muhammad, H. Depner, C. Mettke, J. Buckers, S. W. Hell, M. Muller, G. W. Davis, D. Schmitz, and S. J. Sigrist. 2011. 'RIM-binding protein, a central part of the active zone, is essential for neurotransmitter release', *Science*, 334: 1565-9.

Liu, S., P. Hoess, and J. Ries. 2022. 'Super-Resolution Microscopy for Structural Cell Biology', *Annu Rev Biophys*, 51: 301-26.

Lnenicka, G. A., and H. Keshishian. 2000. 'Identified motor terminals in Drosophila larvae show distinct differences in morphology and physiology', *J Neurobiol*, 43: 186-97.

Los, G. V., L. P. Encell, M. G. McDougall, D. D. Hartzell, N. Karassina, C. Zimprich, M. G. Wood, R. Learish, R. F. Ohana, M. Urh, D. Simpson, J. Mendez, K. Zimmerman, P. Otto, G. Vidugiris, J. Zhu, A. Darzins, D. H. Klaubert, R. F. Bulleit, and K. V. Wood. 2008. 'HaloTag: a novel protein labeling technology for cell imaging and protein analysis', *ACS Chem Biol*, 3: 373-82.

Lu, Z., A. K. Chouhan, J. A. Borycz, Z. Lu, A. J. Rossano, K. L. Brain, Y. Zhou, I. A. Meinertzhagen, and G. T. Macleod. 2016. 'High-Probability Neurotransmitter Release Sites Represent an Energy-Efficient Design', *Curr Biol*, 26: 2562-71.

Ly , Cindy V., Chi-Kuang Yao , Patrik Verstreken , Tomoko Ohyama , and Hugo J. Bellen 2008. 'straightjacket is required for the synaptic stabilization of cacophony, a voltage-gated calcium channel α1 subunit', *Journal of Cell Biology*, 181: 157-70.

Macleod, G. T., L. Chen, S. Karunanithi, J. B. Peloquin, H. L. Atwood, J. E. McRory, G. W. Zamponi, and M. P. Charlton. 2006. 'The Drosophila cacts2 mutation reduces presynaptic Ca2+ entry and defines an important element in Cav2.1 channel inactivation', *Eur J Neurosci*, 23: 3230-44.

McDonald, N. A., R. D. Fetter, and K. Shen. 2020. 'Assembly of synaptic active zones requires phase separation of scaffold molecules', *Nature*, 588: 454-58.

Medeiros, Audrey T., and Kate O'Connor-Giles. 2023. 'To Ib or not to b: Transcriptional regulation of tonic type Ib vs. phasic type Is motor neurons', *Neuron*, 111: 3497-99.

Melom, J. E., Y. Akbergenova, J. P. Gavornik, and J. T. Littleton. 2013. 'Spontaneous and evoked release are independently regulated at individual active zones', *J Neurosci*, 33: 17253-63.

Miki, Takafumi, Walter A. Kaufmann, Gerardo Malagon, Laura Gomez, Katsuhiko Tabuchi, Masahiko Watanabe, Ryuichi Shigemoto, and Alain Marty. 2017. 'Numbers of presynaptic Ca²⁺ channel clusters match those of functionally defined vesicular docking sites in single central synapses', *Proceedings of the National Academy of Sciences*, 114: E5246-E55.

Mrestani, Achmed, Martin Pauli, Philip Kollmannsberger, Felix Repp, Robert J. Kittel, Jens Eilers, Sören Doose, Markus Sauer, Anna-Leena Sirén, Manfred Heckmann, and Mila M. Paul. 2021. 'Active zone compaction correlates with presynaptic homeostatic potentiation', *Cell Reports*, 37: 109770.

Muhammad, K., S. Reddy-Alla, J. H. Driller, D. Schreiner, U. Rey, M. A. Bohme, C. Hollmann, N. Ramesh, H. Depner, J. Lutzkendorf, T. Matkovic, T. Gotz, D. D. Bergeron, J. Schmoranzer, F. Goettfert, M. Holt, M. C. Wahl, S. W. Hell, P. Scheiffele, A. M. Walter, B. Loll, and S. J. Sigrist. 2015. 'Presynaptic spinophilin tunes neurexin signalling to control active zone architecture and function', *Nat Commun*, 6: 8362.

Muller, C. S., A. Haupt, W. Bildl, J. Schindler, H. G. Knaus, M. Meissner, B. Rammner, J. Striessnig, V. Flockerzi, B. Fakler, and U. Schulte. 2010. 'Quantitative proteomics of the Cav2 channel nano-environments in the mammalian brain', *Proc Natl Acad Sci U S A*, 107: 14950-7.

Nakamura, Yukihiro, Harumi Harada, Naomi Kamasawa, Ko Matsui, Jason S Rothman, Ryuichi Shigemoto, R. Angus Silver, David A DiGregorio, and Tomoyuki Takahashi. 2015. 'Nanoscale Distribution of Presynaptic Ca2+ Channels and Its Impact on Vesicular Release during Development', *Neuron*, 85: 145-58.

Newman, Z. L., A. Hoagland, K. Aghi, K. Worden, S. L. Levy, J. H. Son, L. P. Lee, and E. Y. Isacoff. 2017. 'Input-Specific Plasticity and Homeostasis at the Drosophila Larval Neuromuscular Junction', *Neuron*, 93: 1388-404 e10.

Newman, Zachary L., Dariya Bakshinskaya, Ryan Schultz, Samuel J. Kenny, Seonah Moon, Krisha Aghi, Cherise Stanley, Nadia Marnani, Rachel Li, Julia Bleier, Ke Xu, and Ehud Y. Isacoff. 2022. 'Determinants of synapse diversity revealed by super-resolution quantal transmission and active zone imaging', *Nature Communications*, 13: 229.

Öztürk-Çolak, Arzu, Steven J Marygold, Giulia Antonazzo, Helen Attrill, Damien Goutte-Gattat, Victoria K Jenkins, Beverley B Matthews, Gillian Millburn, Gilberto dos Santos, Christopher J Tabone, and FlyBase Consortium. 2024. 'FlyBase: updates to the Drosophila genes and genomes database', *Genetics*, 227.

Paez-Segala, M. G., M. G. Sun, G. Shtengel, S. Viswanathan, M. A. Baird, J. J. Macklin, R. Patel, J. R. Allen, E. S. Howe, G. Piszczek, H. F. Hess, M. W. Davidson, Y. Wang, and L. L. Looger. 2015. 'Fixation-resistant photoactivatable fluorescent proteins for CLEM', *Nat Methods*, 12: 215-8, 4 p following 18.

Peled, E. S., and E. Y. Isacoff. 2011. 'Optical quantal analysis of synaptic transmission in wild-type and rab3-mutant Drosophila motor axons', *Nat Neurosci*, 14: 519-26.

Peled, E. S., Z. L. Newman, and E. Y. Isacoff. 2014. 'Evoked and spontaneous transmission favored by distinct sets of synapses', *Curr Biol*, 24: 484-93.

Peng, I. F., and C. F. Wu. 2007. 'Drosophila cacophony channels: a major mediator of neuronal Ca2+ currents and a trigger for K+ channel homeostatic regulation', *J Neurosci*, 27: 1072-81.

Petersen, Sophie A., Richard D. Fetter, Jasprina N. Noordermeer, Corey S. Goodman, and Aaron DiAntonio. 1997. 'Genetic Analysis of Glutamate Receptors in Drosophila Reveals a Retrograde Signal Regulating Presynaptic Transmitter Release', *Neuron*, 19: 1237-48.

Radulovic, T., W. Dong, R. O. Goral, C. I. Thomas, P. Veeraraghavan, M. S. Montesinos, D. Guerrero-Given, K. Goff, M. Lubbert, N. Kamasawa, T. Ohtsuka, and S. M. Young, Jr. 2020. 'Presynaptic development is controlled by the core active zone proteins CAST/ELKS', *J Physiol*, 598: 2431-52.

Rebola, Nelson, Maria Reva, Tekla Kirizs, Miklos Szoboszlay, Andrea Lőrincz, Gael Moneron, Zoltan Nusser, and David A. Digregorio. 2019. 'Distinct Nanoscale Calcium Channel and Synaptic Vesicle Topographies Contribute to the Diversity of Synaptic Function', *Neuron*, 104: 693-710.e9.

Reddy-Alla, S., M. A. Bohme, E. Reynolds, C. Beis, A. T. Grasskamp, M. M. Mampell, M. Maglione, M. Jusyte, U. Rey, H. Babikir, A. W. McCarthy, C. Quentin, T. Matkovic, D. D. Bergeron, Z. Mushtaq, F. Gottfert, D. Owald, T. Mielke, S. W. Hell, S. J. Sigrist, and A. M. Walter. 2017. 'Stable Positioning of Unc13 Restricts Synaptic Vesicle Fusion to Defined Release Sites to Promote Synchronous Neurotransmission', *Neuron*, 95: 1350-64 e12.

Reuveny, Adriana, Marina Shnayder, Dana Lorber, Shuoshuo Wang, and Talila Volk. 2018. 'M-alpha2/delta promotes myonuclear positioning and association with the sarcoplasmic-reticulum', *Development*, 145: dev159558.

Risher, W. Christopher, Namsoo Kim, Sehwon Koh, Ji-Eun Choi, Petar Mitev, Erin F. Spence, Louis-Jan Pilaz, Dongqing Wang, Guoping Feng, Debra L. Silver, Scott H. Soderling, Henry H. Yin, and Cagla Eroglu. 2018. 'Thrombospondin receptor α2δ-1 promotes synaptogenesis and spinogenesis via postsynaptic Rac1', *Journal of Cell Biology*, 217: 3747-65.

Sauvola, Chad W., Yulia Akbergenova, Karen L. Cunningham, Nicole A. Aponte-Santiago, and J. Troy Littleton. 2021. 'The decoy SNARE Tomosyn sets tonic versus phasic release properties and is required for homeostatic synaptic plasticity', *eLife*, 10: e72841.

Schöpf, Clemens L., Cornelia Ablinger, Stefanie M. Geisler, Ruslan I. Stanika, Marta Campiglio, Walter A. Kaufmann, Benedikt Nimmervoll, Bettina Schlick, Johannes Brockhaus, Markus Missler, Ryuichi Shigemoto, and Gerald J. Obermair. 2021. 'Presynaptic α2δ subunits are key organizers of glutamatergic synapses', *Proceedings of the National Academy of Sciences*, 118: e1920827118.

Sheng, Jiansong, Liming He, Hongwei Zheng, Lei Xue, Fujun Luo, Wonchul Shin, Tao Sun, Thomas Kuner, David T. Yue, and Ling-Gang Wu. 2012. 'Calcium-channel number critically influences synaptic strength and plasticity at the active zone', *Nat Neurosci*, 15: 998-1006.

Smith, L. A., X. Wang, A. A. Peixoto, E. K. Neumann, L. M. Hall, and J. C. Hall. 1996. 'A Drosophila calcium channel alpha1 subunit gene maps to a genetic locus associated with behavioral and visual defects', *J Neurosci*, 16: 7868-79.

Thomas, G. D. 2000. 'Effect of dose, molecular size, and binding affinity on uptake of antibodies', *Methods Mol Med*, 25: 115-32.

Tong, X. J., E. J. Lopez-Soto, L. Li, H. Liu, D. Nedelcu, D. Lipscombe, Z. Hu, and J. M. Kaplan. 2017. 'Retrograde Synaptic Inhibition Is Mediated by alpha-Neurexin Binding to the alpha2delta Subunits of N-Type Calcium Channels', *Neuron*, 95: 326-40 e5.

Voigt, A., R. Freund, J. Heck, M. Missler, G. J. Obermair, U. Thomas, and M. Heine. 2016. 'Dynamic association of calcium channel subunits at the cellular membrane', *Neurophotonics*, 3: 041809.

880 Wang, L. Y., and G. J. Augustine. 2014. 'Presynaptic nanodomains: a tale of two synapses', *Front Cell*
881 *Neurosci*, 8: 455.

882 Wang, T., R. T. Jones, J. M. Whippen, and G. W. Davis. 2016. 'alpha2delta-3 Is Required for Rapid
883 Transsynaptic Homeostatic Signaling', *Cell Rep*, 16: 2875-88.

884 Weiss, N., and G. W. Zamponi. 2017. 'Trafficking of neuronal calcium channels', *Neuronal Signal*, 1:
885 NS20160003.

886 Weyhersmuller, A., S. Hallermann, N. Wagner, and J. Eilers. 2011. 'Rapid active zone remodeling
887 during synaptic plasticity', *J Neurosci*, 31: 6041-52.

888 Yazaki, Junshi, Yusuke Kawashima, Taisaku Ogawa, Atsuo Kobayashi, Mayu Okoshi, Takashi
889 Watanabe, Suguru Yoshida, Isao Kii, Shohei Egami, Masayuki Amagai, Takamitsu Hosoya, Katsuyuki
890 Shiroguchi, and Osamu Ohara. 2019. 'HaloTag-based conjugation of proteins to barcoding-
891 oligonucleotides', *Nucleic Acids Research*, 48: e8-e8.

892 Zhang, Yanfeng, Ting Wang, Yimei Cai, Tao Cui, Michelle Kuah, Stefano Vicini, and Tingting Wang.
893 2023. 'Corrigendum: Role of α2δ-3 in regulating calcium channel localization at presynaptic active
894 zones during homeostatic plasticity', *Frontiers in Molecular Neuroscience*, 16.
895
896

897 **Table S1. Absolute values and statistics.** All comparisons, Ns (animals, NMJs, AZs (AZs), and
898 statistical tests used in this study. All values are mean ± SEM.
899

Figure. Panel	Comparison	Ns	Values/Statistical tests
Fig. 1C	Average P_r in type Ib and type Is	6 animals, 6 NMJs	Ib Average P_r = 12.47 ± 0.88% Is Average P_r = 25.69 ± 1.20% Paired t test, $p < 0.0001$
Fig. 1E	$Cac^{Td\text{-}Tomato\text{-}N}$ to P_r correlation in type Is	6 animals, 6 NMJs	Average type Is Pearson's r = 0.617 ± 0.028
Fig. 1F	$Cac^{Td\text{-}Tomato\text{-}N}$ to P_r correlation in type Ib	6 animals, 6 NMJs	Average type Ib Pearson's r = 0.576 ± 0.035
Fig. 1H	$Cac^{sfGFP\text{-}N}$ levels at type Ib vs type Is	n = 12 animals, 36 NMJs	Type Ib mean: 1.000 ± 0.017 Type Is mean: 0.991 ± 0.028 t test, p = 0.78
Fig. 1J	Slopes of $Cac^{Td\text{-}Tomato\text{-}N}$ to P_r correlation at type Ib vs type Is	6 animals, 6 NMJs Type Ib: n = 531 AZs Type Is: n = 365 AZs	Ib Slope = 0.085 ± 0.006 Is Slope = 0.154 ± 0.011 ANCOVA test, $p < 0.0001$
Fig. 2F	$Cac^{HaloTag\text{-}N}$ cluster area in type Ib and type Is	5 animals, 14 NMJs Type Ib: n = 80 boutons 5 animals, 19 NMJs Type Is: n = 96 boutons	Type Ib = 0.0093 ± 0.0004 μm^2 Type Is = 0.0098 ± 0.0004 μm^2 Mann-Whitney test, p = 0.5906
Fig. 2G	$Cac^{HaloTag\text{-}N}$ localizations per cluster in type Ib and type Is	5 animals, 14 NMJs Type Ib: n = 80 boutons 5 animals, 19 NMJs Type Is: n = 96 boutons	Type Ib = 69.39 ± 4.76 Type Is = 83.52 ± 5.67 Mann-Whitney test, p = 0.0928
Fig. 2H	$Cac^{HaloTag\text{-}N}$ cluster density in type Ib and type Is	5 animals, 14 NMJs Type Ib: n = 80 boutons 5 animals, 19 NMJs Type Is: n = 96 boutons	Type Ib = 7185 ± 234.7 μm^{-2} Type Is = 8277 ± 342.6 μm^{-2} Mann-Whitney test, p = 0.0278
Fig. 2I	$Cac^{HaloTag\text{-}N}$ cluster	Type Ib: n = 5	Type Ib = 7300 ± 362.2 μm^{-2}

	density per NMJ in type Ib and type Is	animals, 14 NMJs Type Is: n = 5 animals 19 NMJs	Type Is = 8569 ± 584.0 μm^{-2} Wilcoxon test, p = 0.0076
Fig. 3B	Brp levels at type Ib and type Is	n = 12 animals, 36 NMJs	Type Ib mean: 1.00 ± 0.02 Type Is mean: 0.79 ± 0.03 Unpaired T-test, p < 0.0001
Fig. 3C	$Cac^{sfGFP-N}$:Brp ratio at type Ib vs type Is	n = 12 animals, 36 NMJs	Type Ib mean: 1.00 ± 0.01 Type Is mean: 1.30 ± 0.05 Paired T-test, p < 0.0001
Fig. 3D	$Cac^{sfGFP-N}$:Brp correlation	12 animals, 36 NMJs Ib: n = 5349 AZs Is: n = 2625 AZs	Type Ib slope: 0.874 ± 0.005 Type Is slope: 0.787 ± 0.009 ANCOVA, p < 0.0001
Fig. 3G	$Cac^{sfGFP-N}$ levels in type Ib vs Is in Control and $brp^{-/-}$	9 animals Control Ib: n = 29 NMJs $brp^{-/-}$ Ib: n = 31 NMJs Control Is: n = 29 NMJs $brp^{-/-}$ Is: n = 31 NMJs	Control Ib mean = 1.00 ± 0.03 $brp^{-/-}$ Ib mean = 0.33 ± 0.01; p < 0.0001 Control Is mean = 1.00 ± 0.03 $brp^{-/-}$ Is mean = 0.45 ± 0.02; p < 0.0001 Kruskal-Wallis test adjusted p values vs Control
Fig. 3H	$brp^{-/-}$:Control ratio of $Cac^{sfGFP-N}$ levels in type Ib vs Is	n = 9 animals, 31 NMJs	Ib ratio = 0.334 ± 0.010 Is ratio = 0.451 ± 0.018 Mann-Whitney test, p < 0.0001
Fig. 4C	Brp levels at $cac^{sfGFP-N}$ type Ib and type Is terminals in control vs PhTx	Control: n = 12 animals, 40 NMJs PhTx: n = 12 animals, 40 NMJs	Control Ib = 1.000 ± 0.047 PhTx Ib = 1.488 ± 0.068; p < 0.0001 Control Is = 1.000 ± 0.050 PhTx Is = 1.493 ± 0.076; p < 0.0001 Kruskal-Wallis test adjusted p values vs Control
Fig. 4D	$Cac^{sfGFP-N}$ levels at $cac^{sfGFP-N}$ type Ib and type Is terminals in control vs PhTx	Control: n = 12 animals, 40 NMJs PhTx: n = 12 animals, 40 NMJs	Control Ib = 1.000 ± 0.044 PhTx Ib = 1.325 ± 0.059; p < 0.0001 Control Is = 1.000 ± 0.048 PhTx Is = 1.300 ± 0.058; p = 0.0002 ANOVA test adjusted p values vs Control
Fig. 4G	$Cac^{sfGFP-N}$ levels at $cac^{sfGFP-N}$; $brp^{-/-}$ type Ib and type Is	Control: n = 12 animals, 43 NMJs	Control Ib = 1.000 ± 0.041 PhTx Ib = 1.029 ± 0.038; p = 0.8475

	terminals in control vs PhTx	PhTx: n = 12 animals, 43 NMJs	Control Is = 1.000 ± 0.046 PhTx Is = 0.8288 ± 0.035; p = 0.0058 ANOVA test adjusted p values vs Control
Fig. 5C	EJPs of endogenously tagged subunits	WT: n = 9 NMJs Stj: n = 8 NMJs Stolid: n = 11 NMJs Ca-β: n = 9 NMJs	WT mean = 30.21 ± 4.09 mV Stj mean = 41.17 ± 4.32 mV; p = 0.14 Stolid mean = 26.44 ± 2.82 mV; p = 0.80 Ca-β mean = 36.49 ± 4.09 mV; p = 0.52 ANOVA, adjusted p values vs WT
Fig. 5D	mEJPs of endogenously tagged subunits	WT: n = 9 NMJs Stj: n = 8 NMJs Stolid: n = 11 NMJs Ca-β: n = 9 NMJs	WT mean = 1.02 ± 0.08 mV Stj mean = 1.12 ± 0.07 mV; p = 0.92 Stolid mean = 1.11 ± 0.09 mV; p = 0.99 Ca-β mean = 1.16 ± 0.09 mV; p = 0.57 Kruskal-Wallis test adjusted p values vs WT
Fig. 5E	QC of endogenously tagged subunits	WT: n = 9 NMJs Stj: n = 8 NMJs Stolid: n = 11 NMJs Ca-β: n = 9 NMJs	WT mean = 29.63 ± 2.96 Stj mean = 37.02 ± 3.93; p = 0.34 Stolid mean = 24.73 ± 2.63; p = 0.60 Ca-β mean = 32.79 ± 4.34; p = 0.86 ANOVA, adjusted p values vs WT
Fig. 6E	Ca-$\beta^{V5\text{-}C}$ levels at type Ib vs type Is	n = 11 animals, 27 NMJs	Type Ib mean: 1.00 ± 0.04 Type Is mean: 0.90 ± 0.04 Mann-Whitney Test, p = 0.06
Fig. 6F	$Stj^{V5\text{-}N}$ levels at type Ib vs type Is	n = 9 animals, 28 NMJs	Type Ib mean: 1.00 ± 0.05 Type Is mean: 0.76 ± 0.05 Unpaired t test, p = 0.0008
Fig. 6G, H	$Cac^{sfGFP\text{-}N}$:$Stj^{V5\text{-}N}$ correlation	5 animals, 22 NMJs Ib: n = 4012 AZs Is: n = 2211 AZs	Type Ib slope: 0.912 ± 0.009 Type Is slope: 0.914 ± 0.012 ANCOVA, p = 0.90
Fig. 7C	$Stj^{V5\text{-}N}$ levels at type Ib and type Is terminals in control vs PhTx	Control: n = 6 animals, 34 NMJs PhTx: n = 6 animals, 26 NMJs	Control Ib = 1.00 ± 0.01 PhTx Ib = 1.27 ± 0.03; p < 0.0001 Control Is = 1.00 ± 0.02 PhTx Is = 1.26 ± 0.02; p < 0.0001 Kruskal-Wallis test adjusted p values vs Control
Fig. 7F	$Stj^{V5\text{-}N}$ levels at type Ib and type Is terminals in control	Control: n = 7 animals, 37 NMJs	Control Ib = 1.00 ± 0.02 *GluRIIA*$^{-/-}$ Ib = 1.18 ± 0.03; p < 0.0001

	vs *GluRIIA*$^{-/-}$	*GluRIIA*$^{-/-}$: n = 7 animals, 26 NMJs	Control Is = 1.00 ± 0.02 *GluRIIA*$^{-/-}$ Is = 1.17 ± 0.03; p < 0.0001 ANOVA test adjusted p values vs Control
Fig. S1D	EJPs of Cac endogenous tags	Control: n = 11 NMJs *cac*$^{HaloTag\text{-}N}$: n = 8 NMJs *cac*$^{Td\text{-}Tomato\text{-}N}$: n = 8 NMJs	Control mean = 42.51 ± 2.08 mV *cac*$^{HaloTag\text{-}N}$ mean = 43.02 ± 1.92 mV; p = >0.99 *cac*$^{Td\text{-}Tomato\text{-}N}$ mean = 40.07 ± 0.99 mV; p = 0.25 Kruskal-Wallis test adjusted p values vs Control
Fig. S1E	mEJPs of Cac endogenous tags	Control: n = 11 NMJs *cac*$^{HaloTag\text{-}N}$: n = 8 NMJs *cac*$^{Td\text{-}Tomato\text{-}N}$: n = 8 NMJs	Control mean = 0.88 ± 0.07 mV *cac*$^{HaloTag\text{-}N}$ mean = 0.77 ± 0.07 mV; p = 0.47 *cac*$^{Td\text{-}Tomato\text{-}N}$ mean = 0.93 ± 0.06 mV; p = 0.86 ANOVA, adjusted p values vs Control
Fig. S1F	QC of Cac endogenous tags	Control: n = 11 NMJs *cac*$^{HaloTag\text{-}N}$: n = 8 NMJs *cac*$^{Td\text{-}Tomato\text{-}N}$: n = 8 NMJs	Control mean = 49.97 ± 2.56 mV *cac*$^{HaloTag\text{-}N}$ mean = 59.83 ± 6.76 mV; p = 0.23 *cac*$^{Td\text{-}Tomato\text{-}N}$ mean = 44.34 ± 2.95 mV; p = 0.60 ANOVA, adjusted p values vs Control

900

901 **Table S2. Imaging details.** This table contains detailed information on how each protein was labeled
902 and visualized using live and fixed confocal microscopy and STORM imaging. All secondary antibodies
903 were incubated at RT for 2 hours at a concentration of 1:500.
904

Imaging Method	Protein	Genetic line	Imaging Reagents	Sample processing
Confocal	Cac	*cac*$^{sfGFP-N}$ (Gratz et al., 2019)	anti-GFP AF488 conjugate (ThermoFisher- RRID:AB_221477)	Fix: Bouins or 4% PFA Staining: 1:500, 2 hours at RT
Confocal	Stj	*stj*$^{V5-N}$ (this study)	*Primary:* anti-V5 monoclonal (ThermoFisher- RRID:AB_2556564) *Secondary:* Goat anti-Mouse IgG Highly Cross-Adsorbed AF488 (ThermoFisher- RRID:AB_2534088)	Fix: Methanol Primary staining: 1:500, overnight at 4°C *Note, best in 488 channel
Confocal	Stolid	*stolid*$^{V5-N}$ (this study)	*Primary:* anti-V5 monoclonal (ThermoFisher- RRID:AB_2556564) *Secondary:* Goat anti-Mouse IgG Highly Cross-Adsorbed AF488 (ThermoFisher- RRID:AB_2534088)	Fix: Bouins Primary staining: 1:500, overnight at 4°C
Confocal	Ca-β	*Ca-β*$^{V5-C}$ (this study)	*Primary:* anti-V5 monoclonal (ThermoFisher- RRID:AB_2556564) *Secondary:* Goat anti-Mouse IgG Highly Cross-Adsorbed AF488 (ThermoFisher- RRID:AB_2534088)	Fix: Bouins Primary staining: 1:500, overnight at 4°C
Confocal	Brp		*Primary:* anti-Brp (DSHB- RRID:AB_2314866) *Secondary:* Goat anti-Mouse IgG Highly Cross-Adsorbed AF568 (ThermoFisher- RRID:AB_144696)	Fix: Bouins or Methanol Primary staining: 1:100 overnight at 4°C
Confocal	HRP		anti-HRP AF488 conjugate (Jackson ImmunoResearch- RRID:AB_2338965), anti-HRP AF647 conjugate (Jackson ImmunoResearch- RRID:AB_2338967)	Fix: Bouins or Methanol Primary staining: 1:500, 2 hours at RT

Live Imaging	Cac	*cac*$^{Td\text{-}Tomato\text{-}N}$ (this study)		
STORM	Cac	*cac*$^{HaloTag\text{-}N}$ (this study)	JaneliaFluor 646 HaloTag Ligand (Promega #GA1120)	Live label: 500nM for 20 min in dark box at RT Fix: 4% PFA for 30 min at RT in dark box

905

Figure 1

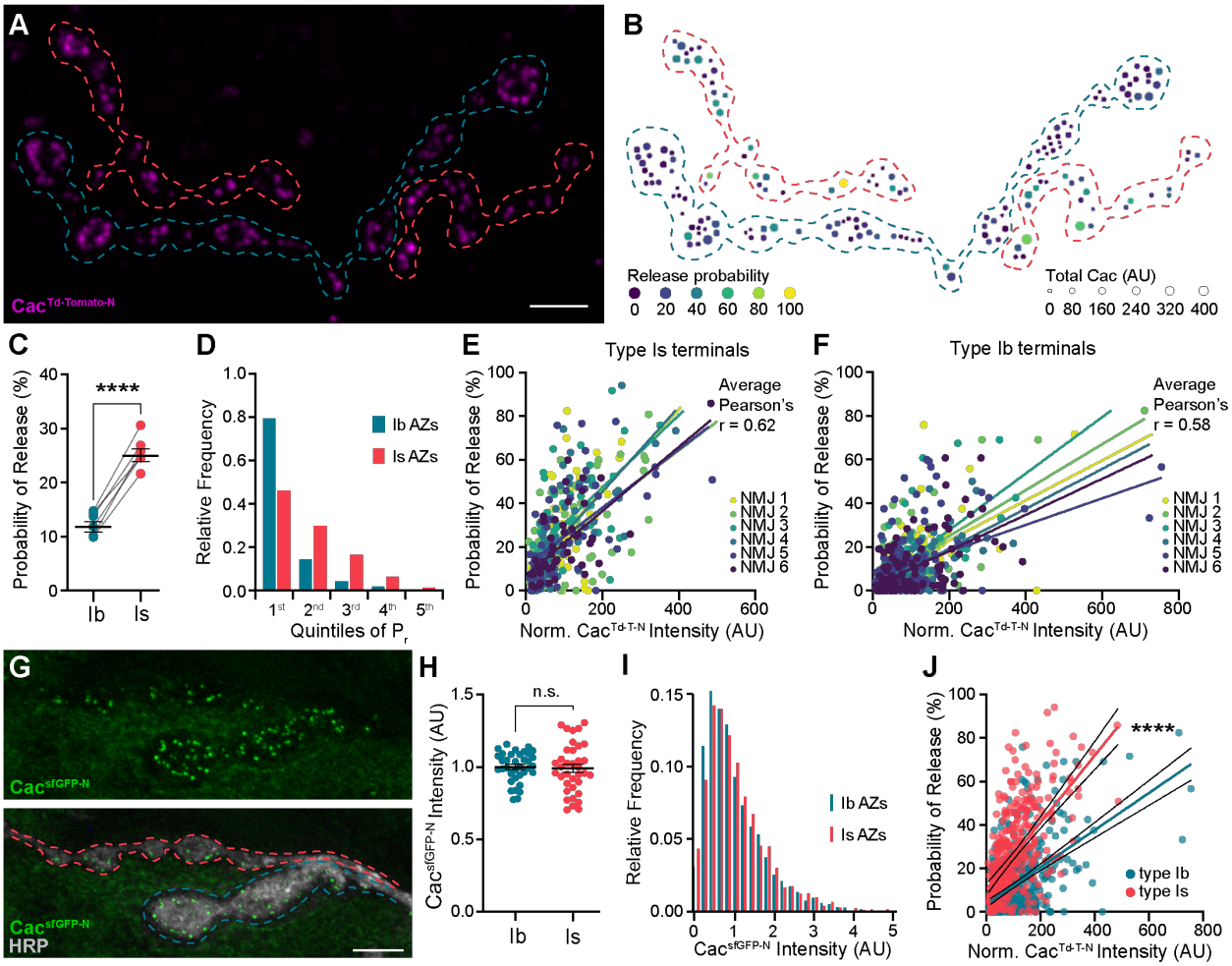

Figure 1: VGCC levels predict P_r within, but not between, inputs.

(A) Representative confocal Z-projection of $Cac^{Td\text{-}Tomato\text{-}N}$ (magenta) with type Ib (blue) and type Is (red) terminals outlined. **(B)** AZ heat map of terminals in A with color indicating P_r and size representing sum Cac intensity levels in arbitrary units (AU). **(C)** Average single-AZ probability of release at type Ib and Is terminals. **(D)** Quintile distribution of single-AZ P_r frequency at type Ib and Is inputs. **(E, F)** Correlation between normalized $Cac^{Td\text{-}Tomato\text{-}N}$ intensity and P_r at type Is and Ib AZs of the same 6 NMJs. Each dot represents a single AZ and each color corresponds to an individual NMJ with

linear regression lines indicated for each. **(G)** Top, representative confocal Z-projection of $Cac^{sfGFP-N}$. Bottom, $Cac^{sfGFP-N}$ in green with HRP marking neuronal membranes in gray. Type Ib (blue) and type Is (red) terminals are outlined. **(H)** Quantification of $Cac^{sfGFP-N}$ AZ intensity at type Ib and Is terminals. Each data point represents the average normalized single AZ sum intensity for an individual NMJ. **(I)** Distribution of normalized $Cac^{sfGFP-N}$ intensity from single type Ib and Is AZs in H (X-axis cutoff at 5.0). **(J)** Comparison between normalized $Cac^{Td-Tomato-N}$ and P_r of type Ib and Is AZs combined from E-F with linear regression lines (blue and red, respectively) and 95% confidence intervals (black lines) indicated. All scale bars = 5μm.

Figure 2

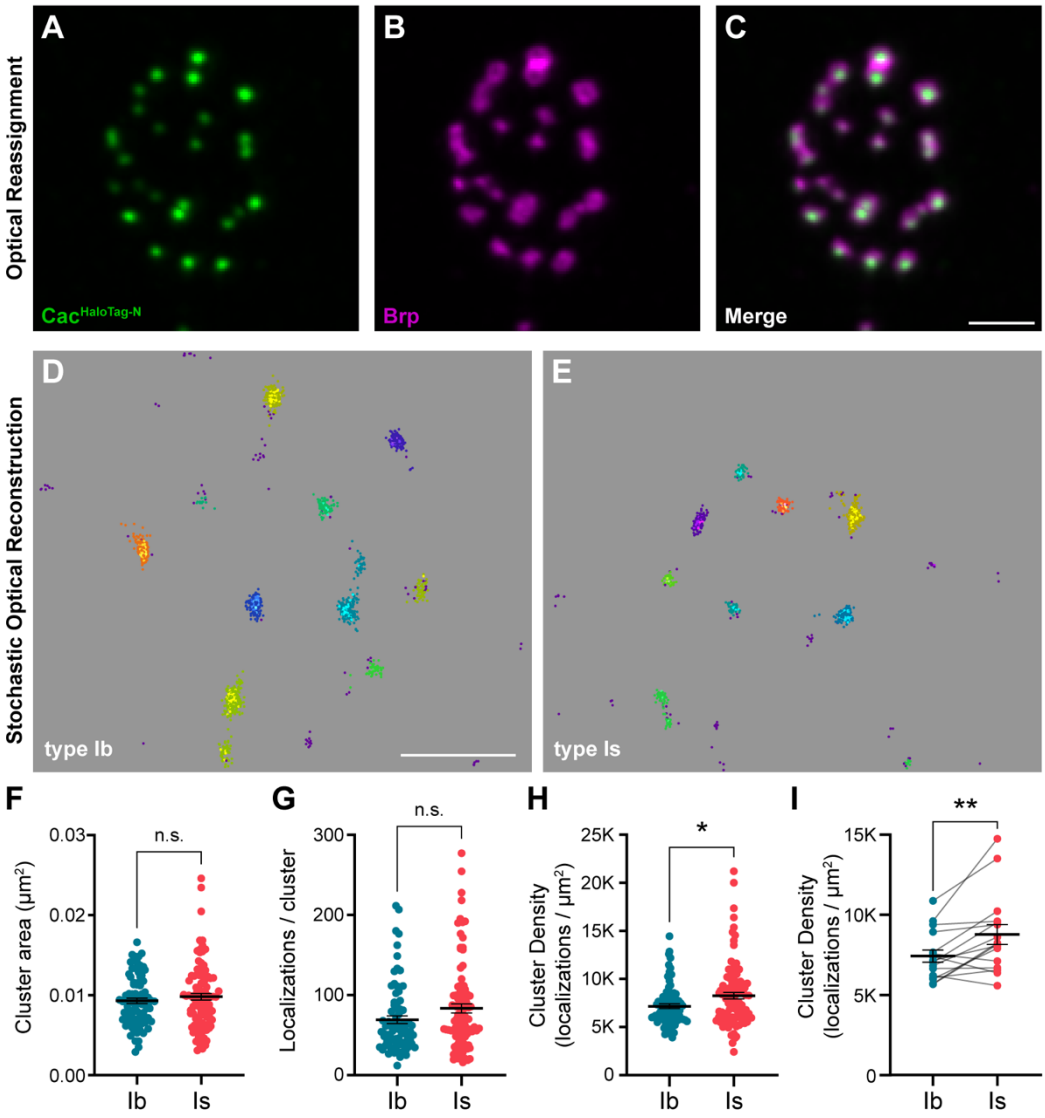

Figure 2: VGCC clusters are more compact at AZs of high-P_r type Is inputs.

(A-C) Representative SoRa Z-projection of $Cac^{HaloTag\text{-}N}$ (green), Brp (magenta), and merge. **(D, E)** Representative boutons of STORM $Cac^{HaloTag\text{-}N}$ clusters as identified by DBSCAN at type Ib and Is boutons as indicated. Each color represents an individual identified cluster with purple scattered dots identifying excluded background signal. **(F-H)** Analysis of STORM-acquired $Cac^{HaloTag\text{-}N}$ clusters where each data point represents the respective single-cluster measurement averaged over individual boutons. **(F)**

Quantification of $Cac^{HaloTag\text{-}N}$ cluster area at type Ib and Is AZs. **(G)** Quantification of localizations per cluster at type Ib and Is boutons. **(H)** Calculated $Cac^{HaloTag\text{-}N}$ cluster density at type Ib and Is AZs. **(I)** Paired analysis of calculated AZ cluster density averaged over individual type Ib and Is inputs to the same muscle. All scale bars = 1μm.

Figure 3

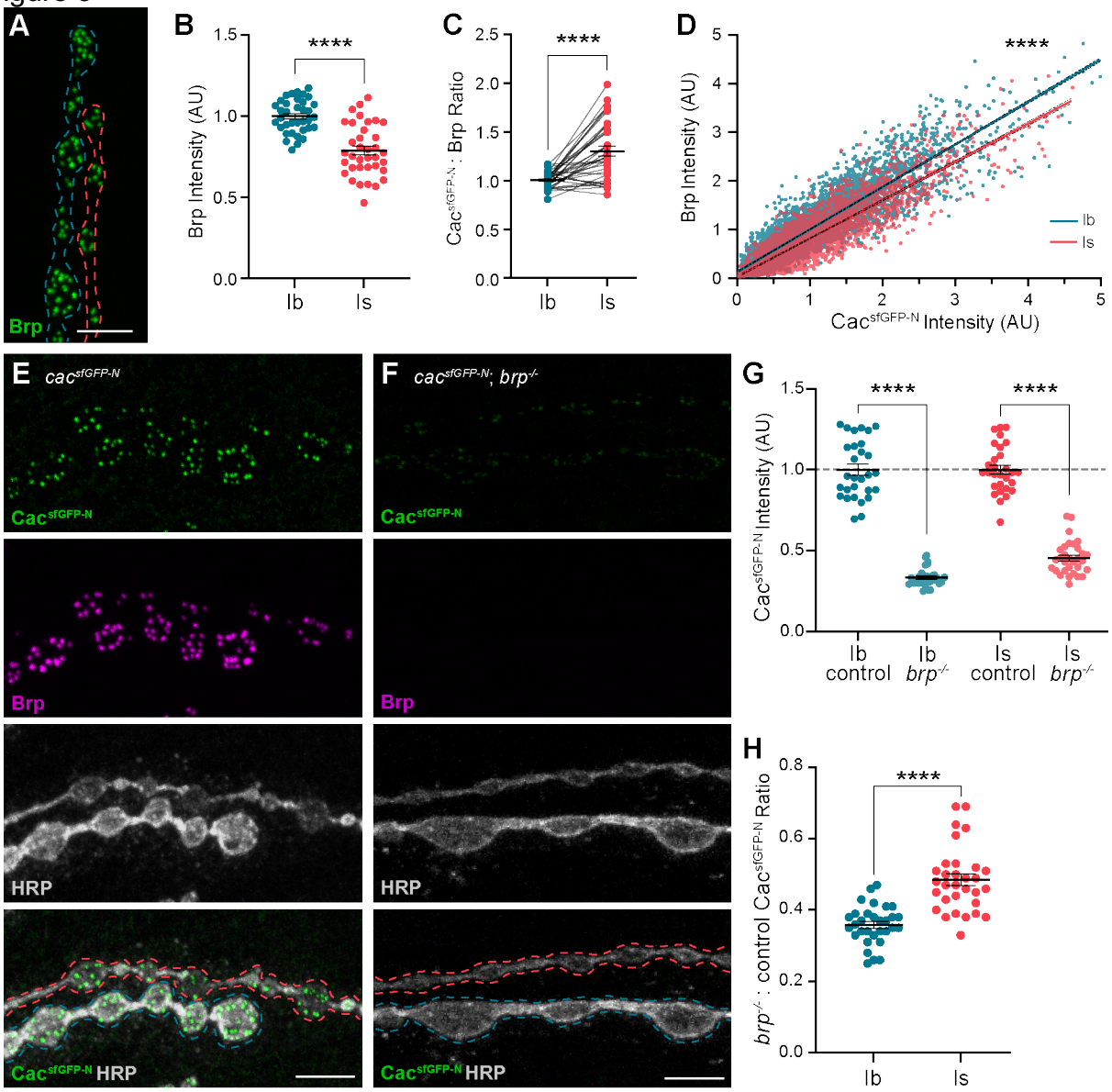

Figure 3: Differences in Bruchpilot (Brp) levels and function at low-and high-P_r inputs.

(A) Representative confocal Z-projection of Brp expression at type Ib (blue outline) and type Is (red outline) terminals. **(B)** Quantification of Brp AZ intensity at type Ib and Is terminals. **(C)** Ratio of normalized $Cac^{sfGFP\text{-}N}$:Brp levels at type Ib and Is inputs to the same muscles. **(D)** Correlation of $Cac^{sfGFP\text{-}N}$ and Brp at type Ib and Is single AZs with linear regression lines (blue and red, respectively) and 95% confidence intervals (black

dotted lines) indicated. **(E, F)** Representative confocal Z-projections of $Cac^{sfGFP-N}$ (green), Brp (magenta), HRP (white), and merge at type Ib (blue outline) and Is (red outline) terminals of *cac*$^{sfGFP-N}$ (control) or *cac*$^{sfGFP-N}$;*brp*$^{-/-}$ (*brp*$^{-/-}$) animals. **(G)** Quantification of $Cac^{sfGFP-N}$ normalized fluorescence intensity at type Ib and Is AZs of control vs *brp*$^{-/-}$ NMJs. **(H)** Ratio of $Cac^{sfGFP-N}$ fluorescence intensity at type Ib and Is AZs between *brp*$^{-/-}$and control NMJs. For B and G, each data point represents the average normalized single AZ sum intensity for an individual NMJ. All scale bars = 5μm.

Figure 4

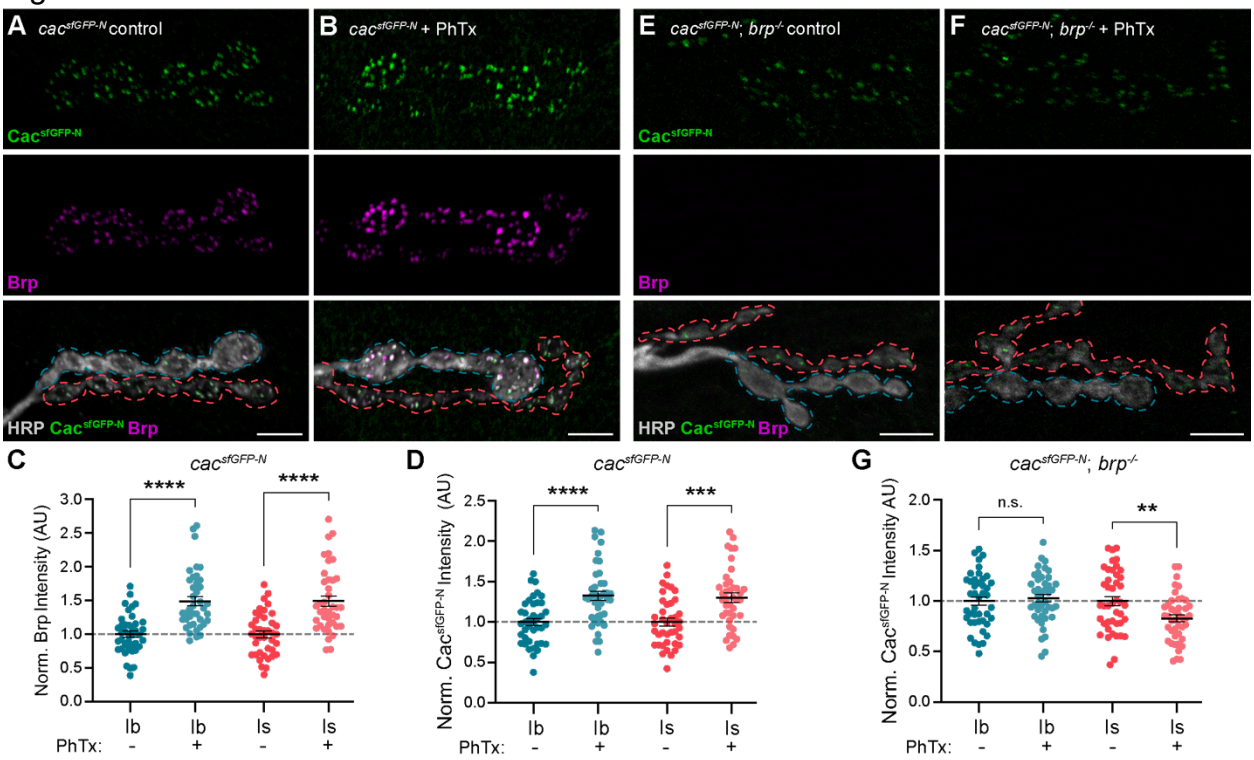

Figure 4: Brp differentially regulates VGCC dynamics at low-and high-P_r inputs during presynaptic homeostatic potentiation.

(A, B) Representative confocal Z-projections of Cac$^{sfGFP-N}$ (top, green), Brp (middle, magenta), and both merged with HRP (bottom, gray) at untreated and PhTx-treated *cac$^{sfGFP-N}$* NMJs showing type Ib (blue) and type Is (red) terminals. **(C)** Quantification of Brp fluorescence intensity at untreated and PhTx-treated type Ib and Is terminals. **(D)** Quantification of Cac$^{sfGFP-N}$ fluorescence intensity at untreated and PhTx-treated type Ib and Is terminals. **(E, F)** Representative confocal Z-projections of Cac$^{sfGFP-N}$ (top, green), Brp (middle, magenta), and both merged with HRP (bottom, gray) at untreated and PhTx-treated *cac$^{sfGFP-N}$;brp$^{-/-}$* NMJs showing type Ib (blue) and type Is (red) terminals. **(G)** Quantification of Cac$^{sfGFP-N}$ fluorescence intensity at untreated and PhTx-treated *cac$^{sfGFP-N}$;brp$^{-/-}$* type Ib and Is terminals. For all quantifications, each data point

represents the average normalized single AZ sum intensity for an individual NMJ. All scale bars = 5μm.

Figure 5

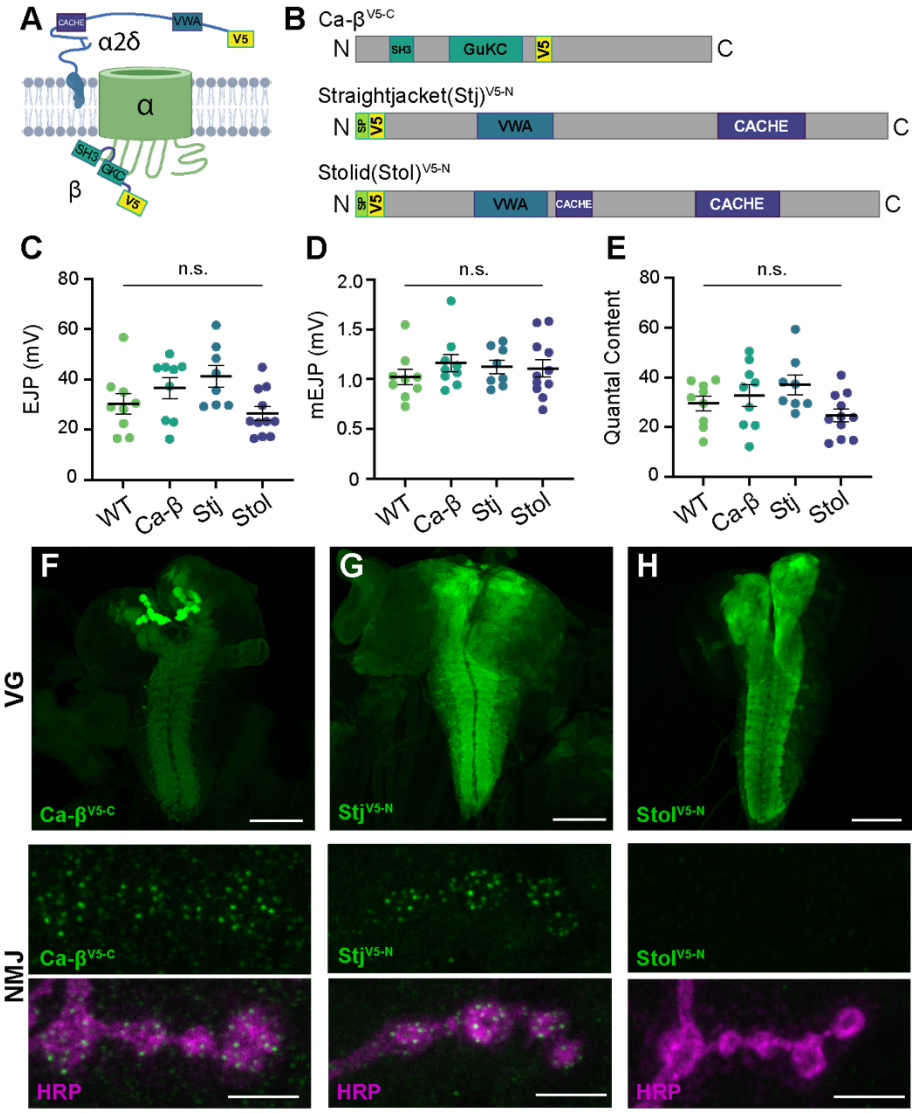

Figure 5: Endogenous tagging of VGCC auxiliary subunits reveals distinct synaptic expression patterns.

(A) Schematic of a Ca^{2+} channel complex with tagged auxiliary subunits (created with BioRender). **(B)** Schematic of Ca-β (isoform PL shown), Stj (isoform PC), and Stolid (isoform H/I) indicating endogenous tag locations. **(C-E)** Quantification of EJPs, mEJPs, and quantal content for each endogenously tagged line. **(F-H)** Representative confocal

Z-projections of auxiliary subunit expression (green) at the larval ventral ganglion (VG, top, scale bars = 100μm) and NMJs co-labeled with anti-HRP (magenta, bottom, scale bars = 5μm).

Figure 6

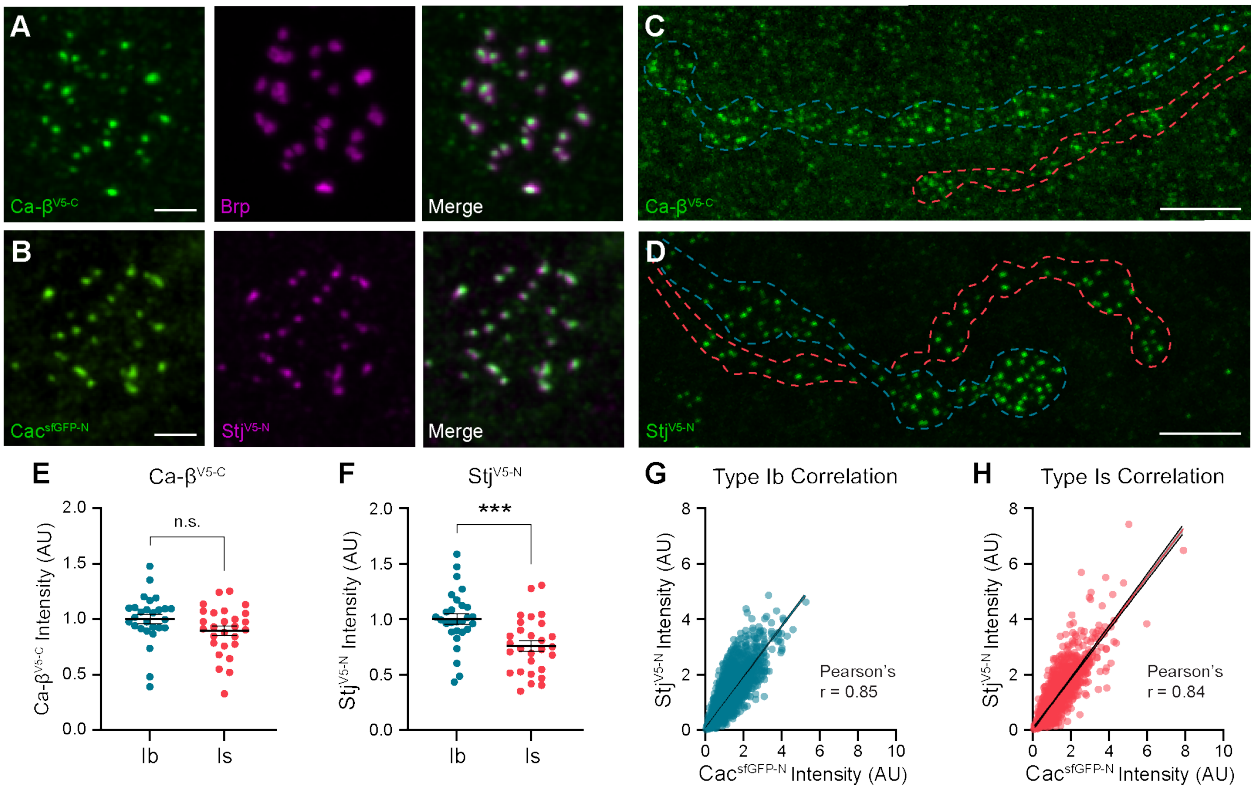

Figure 6: Stj/α2δ-3 levels are lower at AZs of high-P_r type Is inputs.

(A) Representative SoRa Z-projections of Ca-β^{V5-C} (green), Brp (magenta), and merge at a single bouton. **(B)** Representative SoRa Z-projections of Cac$^{sfGFP-N}$ (green), Stj^{V5-N} (magenta), and merge at a single bouton. Scale bars for A and B = 1µm. **(C, D)** Representative confocal Z-projections of Ca-β^{V5-C} expression and Stj^{V5-N} expression at type Ib (blue outline) and type Is (red outline) terminals. Scale bars = 5µm. **(E, F)** Quantification of Ca-β^{V5-C} and Stj^{V5-N} fluorescence intensity at type Ib and Is AZs. Each data point represents the average normalized single AZ sum intensity for an individual NMJ. **(G, H)** Correlation of Cac$^{sfGFP-N}$ and Stj^{V5-N} fluorescence intensity levels at type Ib and Is single AZs with linear regression lines (blue or red line, respectively) and 95% confidence intervals (black lines).

Figure 7

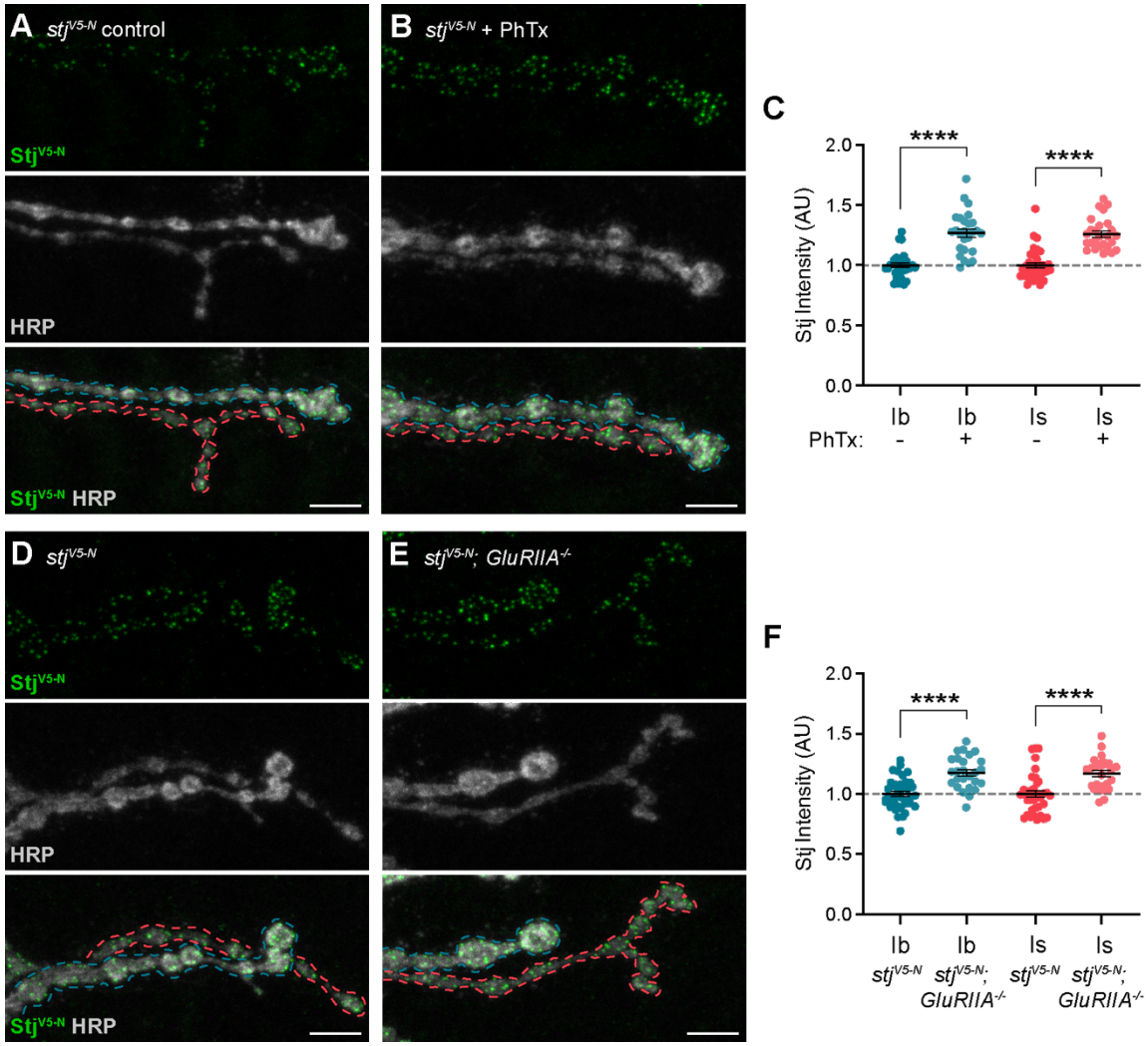

Figure 7: Stj/α2δ-3 levels are modulated at AZs of both low- and high-P_r inputs during presynaptic homeostatic potentiation.

(A, B) Representative confocal Z-projections of $Stj^{V5\text{-}N}$ (top, green), HRP (middle, gray), and merge (bottom) at untreated and PhTx-treated *$stj^{V5\text{-}N}$* NMJs showing type Ib (blue) and type Is (red) terminals. **(C)** Quantification of $Stj^{V5\text{-}N}$ fluorescence intensity at untreated and PhTx-treated type Ib and Is terminals. **(D-E)** Representative confocal Z-projections of $Stj^{V5\text{-}N}$ (top, green), HRP (middle, gray), and merge (bottom) at *$stj^{V5\text{-}N}$* and *$stj^{V5\text{-}N}$;$GluRIIA^{-/-}$* NMJs showing type Ib (blue) and type Is (red) terminals. **(F)**

Quantification of $Stj^{V5\text{-}N}$ fluorescence intensity levels at $stj^{V5\text{-}N}$ and $stj^{V5\text{-}N}$;$GluRIIA^{-/-}$ type Ib and Is terminals. For all quantifications, each data point represents the average normalized single AZ sum intensity for an individual NMJ. All scale bars = 5μm.

Figure S1

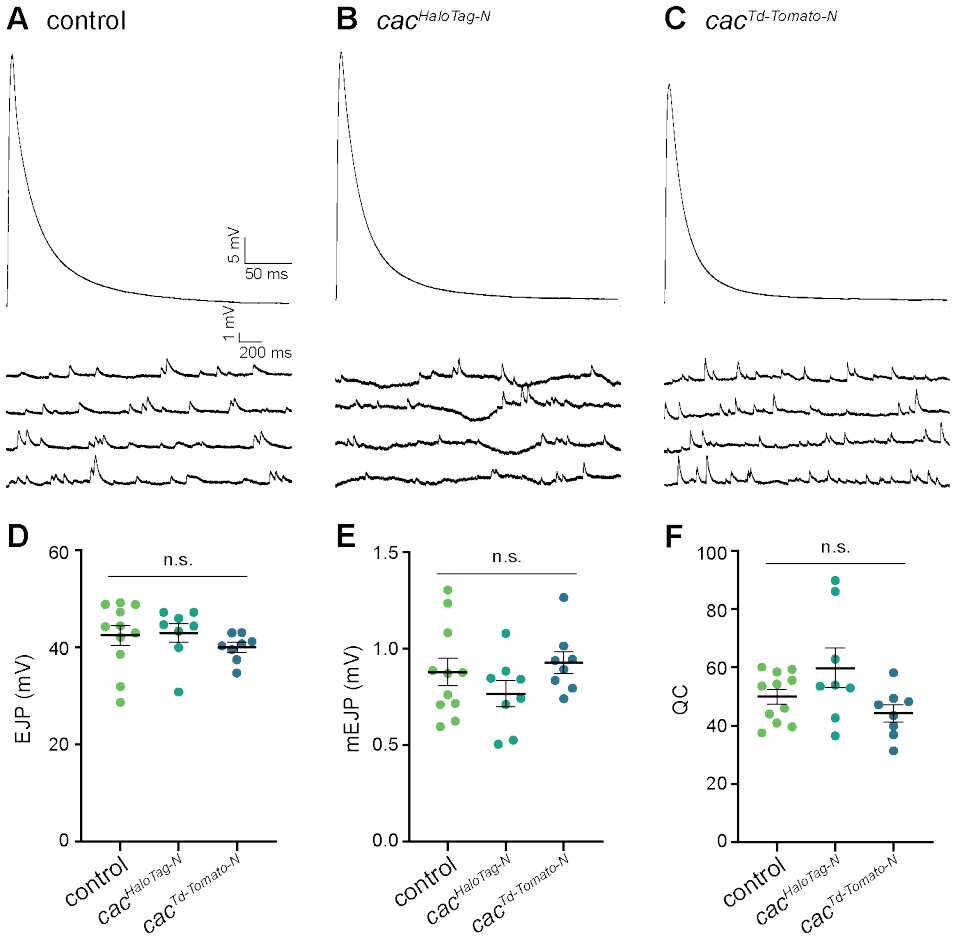

Figure S1: Electrophysiological validation of endogenously tagged cacophony lines. **(A-C)** Representative traces of EJPs (top) and mEJPs (bottom) in control, *cac*$^{HaloTag\text{-}N}$, and *cac*$^{Td\text{-}Tomato\text{-}N}$. **(D-F)** Quantification of EJPs, mEJPs, and quantal content (QC).